Summer 8-8-2017

Near-Field Nanoscale Spectroscopy and Imaging of Enveloped Virus Particles and Layered Materials

Don Sampath Gamage

NEAR-FIELD NANOSCALE SPECTROSCOPY AND IMAGING OF ENVELOPED VIRUS PARTICLES AND LAYERED MATERIALS

by

Don Ruwan Sampath Gamage

Under the Direction of Yohannes Abate, PhD

ABSTRACT

Deeper understanding and technological progress in materials physics demand exploration of soft and hard matter at their relevant length scales. This research focuses on the nanometer length scale investigation of structural changes required for membrane fusion in virus nanoparticles and nano-spectroscopic investigation of layered material surfaces implementing scattering type scanning near-field optical microscopy (s-SNOM).

Spectroscopy and imaging experiments were deployed to investigate the chemical and structural modifications of the viral protein and lipid bilayer under various environmental pH variations. It has been shown that breakage of viral membrane could occur even without the presence of a targeting membrane, if the environment pH is lowered. This is in contrary to the current viral fusion model, which requires virus binding to a host cell membrane for forming the fusion pore to

release the viral genome. The fusion inhibitor compound 136 can effectively prevent the membrane breakage induced by low pH.

The chemical surface stability and degradation of black phosphorus (BP) under ambient conditions have been studied using s-SNOM. We found that the degraded area and volume on the surface of black phosphorus increase with time slowly at the start of degradation and enlarge rapidly (roughly exponentially) afterward and reach saturation growth following S-shaped growth curve (sigmoid growth curve). The theoretical model presented suggests that the degraded sites in the adjacent surrounding causes the experimentally observed exponential growth of degraded area at the initial stage. By studying the BP surfaces coated by Al_2O_3, boron nitride (BN) and hybrid BN/Al_2O_3 layers through the period up to 6 months, it has been concluded that ~5 nm thin hybrid layer of BN/Al_2O_3 helps the surface passivation of BP flakes of thickness ~30 nm. This is supported by the electrical characterization results of BP field effect transistor coated with a BN/Al_2O_3 layer.

We have performed infrared nano-spectroscopy on muscovite mica exfoliated on silicon and silicon dioxide substrates. We show that the near-field profile in s-SNOM can penetrate down to several hundreds of nanometers and enable spectroscopy of buried structures. We found spectral broadening of mica as its thickness increases revealing clearly the effect of size on the absorption response.

INDEX WORDS: Nano-optics, SNOM, Nano-imaging, Nano-FTIR, Influenza virus, TMDC

NEAR-FIELD NANOSCALE SPECTROSCOPY AND IMAGING OF ENVELOPED VIRUS PARTICLES AND LAYERED MATERIALS

by

DON RUWAN SAMPATH GAMAGE

A Dissertation Submitted in Partial Fulfillment of the Requirements for the Degree of

Doctor of Philosophy

in the College of Arts and Sciences

Georgia State University

2017

NEAR-FIELD NANOSCALE SPECTROSCOPY AND IMAGING OF ENVELOPED VIRUS PARTICLES AND LAYERED MATERIALS

by

DON RUWAN SAMPATH GAMAGE

Committee Chair: Yohannes Abate

Committee: A. G. Unil Perera

Ramesh Mani

Vadym Apalkov

Misty Bentz

Electronic Version Approved:

Office of Graduate Studies

College of Arts and Sciences

Georgia State University

August 2017

DEDICATION

To my beloved parents

for their tireless effort to make me who I am today!

ACKNOWLEDGEMENTS

I would like to express my sincere gratitude to my advisor Prof. Yohannes Abate. It would not have been possible for me to achieve the results that I am presenting in this dissertation without his guidance, insightful suggestions and cutting-edge research tools made available to me. I learned from him how to execute academic research, how to collect and interpret data in a consistent way, and specifically how to complete a research project in a given limited time. I was extremely fortunate to have the privilege to work in his group and I honestly believe that the best decision I made in my life as a graduate student was to join his distinguished research group.

I owe special thanks to our collaborators, Prof. Ming Luo at Department of Chemistry of Georgia State University, Prof. Han Wang and Prof. Stephen Cronin at University of Southern California, and Prof. Peide Ye at Purdue University for providing me all the samples needed and for offering valuable comments and suggestions in order to make this work productive and conclusive. Also my special thanks go to Prof Mark Stockman, Dr. Vladislav Yakovlev, Dr. Viktoriia Babicheva and Dr. Mohammad Javani for their contributions in theoretical/computational parts of my research work.

I would like to thank other committee members, Prof. A. G. U. Perera, Prof. Ramesh Mani, Prof. Vadym Apalkov and Prof. Misty Bentz for participating in my dissertation committee and providing helpful comments and suggestions.

My sincere thank goes to Prof. Nikolaus Dietz for his guidance and advice during my early years as a graduate student introducing me to advance scientific research. I am also grateful to my senior student in his group Dr. Max Bugler for training me as a fresh student.

My heartiest gratitude goes to present graduate director Prof. Xiochun He and former director Prof. A.G.U. Perera for their advice and guidance during critical transition from my master program to PhD program.

I would like to thank all of my group members and fellow graduate students of the department of physics for helping me at various occasions during my studies and research work.

Finally yet importantly, I would like to acknowledge funding agencies, Air Force Office for Scientific Research (AFOSR) and National Science Foundation (NSF) for financially supporting this research project.

TABLE OF CONTENTS

LIST OF FIGURES

1 INTRODUCTION

The science and technology of the 21st century has evolved to a state where its advancement primarily depends on how we understand and manipulate the interactions of light with matter at all spatial scales. For a large number of applications that are critical to the semiconductor industry, molecular biology, material science, biochemistry and many other scientific fields, the interaction of light with matter at nanoscale plays a critical role. This was largely a driving force for the emergence of the field of nano-optics. Nano-optics attracted the scientific community across disciplines due to its rapidly increasing scientific importance and technological relevance owing to its applications in fields such as single molecular imaging and spectroscopy, chemical sensing, superlensing, optical computing, optoelectronics, biological light harvesting, and artificial photovoltaic devices.

Nano-optical techniques play a crucial role in understanding basic science as well as in advancing new technologies for both nanoimaging and nanospectroscopy. In particular, microbiology and biochemistry are two areas that these techniques are extensively applied for chemical and structural analysis of organic and biological species at the cellular and molecular level in ambient or even in aqueous environments.

Detailed understanding of viral infection at a single virus level is a key breakthrough in studying virus replication. The entry process of an enveloped virus to a host cell occurs via multiple steps that are accompanied by significant structural and functional modifications of both the viral and the host cellular membranes. Following reduction of luminal pH that causes conformational changes in viral protein hemagglutinin (HA), membrane fusion begins in the endosome in influenza virus infection. The viral protein HA is commonly understood to play a major role in facilitating influenza virus entry into host cells by enabling virus binding and membrane fusion

which successively lead to entry and release of the viral genome. Understanding this complex sequential fusion mechanism offers a tremendous opportunity to design antiviral compounds tuned to interrupt the cascade of events leading to viral infection. Conventional ensemble fusion assays relay on collective responses of fusion events and as a result cannot allow direct quantification of some of the subtle intricate fusion details that are only accessible via single particle isolated studies. In recent years, the scientific community has seen remarkable 'resolution revolution' in the development of super-resolution fluorescence nanoscopy techniques for single molecule manipulation such as stimulated emission depletion (STED) and various other types. These novel super-resolution microscopy techniques provide spatial resolution not limited by diffraction but by fluorophore's properties. As a result, we are witnessing remarkable progress in nanoscale disclosure of virus replication and cell biology. However, limited efficiency of fluorescent labeling methods and limited photon output, on-off switching contrast and duty cycle of fluorescent labels are still challenges that require major improvements. Furthermore, investigation of effects due to real time environmental changes such as pH modifications are not possible by these techniques since such changes also modify the label. In addition, viral mechanical properties and the effect of capsid structural modifications cannot be studied with these techniques. Appropriate single virus particle interrogation tools that not only offer high spatial resolution but also possess the capability to probe mechanical/chemical properties and effects of environmental changes could highly facilitate unprecedented understanding of viral membrane fusion.

Layered materials such as graphene [33, 34], boron nitride (BN) [35, 36], transition metal dichalcogenides (TMDCs) [36-40], layered oxides [1], BP [36, 41-45] and topological insulators [6] have intriguing electronic properties that allow them to interact with light in wide regions of the electromagnetic spectrum and bear promise for numerous applications in electronics and

optics. Many-body interactions are generally more significant in two dimensional (2D) materials than in their bulk counterparts [46] and as a result many novel properties and emergent phenomena of 2D layered materials have been discovered which include spin-valley coupled effects, magnetoelectric effects,[21] surface tuning of band structure, topological quantum phase transitions [47] and spin-polarized electron mobility.[7, 9, 48] Due to these fascinating properties, nano-scale interaction of light with these materials and their heterostructures has become a field of extensive research.

This thesis presents experimental nanoscopic investigation of light–matter interaction in enveloped virus (influenza-A) and layered materials (black phosphorus (BP) and muscovite mica) using the scattering type scanning near-field optical microscope (s-SNOM). Experimental work is supported by theoretical calculations..

1.1 Introduction to Nano-optics

Optical microscopy has played a crucial role in exploring the detailed phenomena in the fields of biology and material science. However, the major limitation in classical optical microscopy is the diffraction barrier that arises from the size of the spot to which a light beam can be focused with normal optical components. In 1873, German physicist Ernst Abbe studied the symmetric pattern (see fig. 1) of concentric rings formed by a light beam at the focal point; these

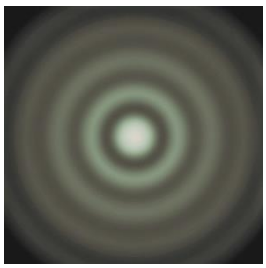

Figure 1.1 An Airy disk pattern.

patterns are known as Airy disk patterns that are named after the English astronomer Sir George Biddell Airy for his significant contribution in understanding these patterns.

Abbe revealed that the distance, d, from the center spot of the disc pattern, to the first minimum in intensity is given by

$$d = \frac{0.6098\lambda}{n \cdot sin\theta} = \frac{0.6098\lambda}{NA} \tag{1.1}$$

where λ is the wavelength of light in vacuum, *n* is the refractive index of the medium in which the light travels, and θ is the collection angle of light for the converging element[1]. The product $n \cdot sin\theta$ is also called the numerical aperture (NA) for the converging element. The Equation (1.1) plays a critical role in determining the resolution: for two distinct objects to be resolvable, they are required to be separated by a distance at least the distance *d* given in equation (1.1).

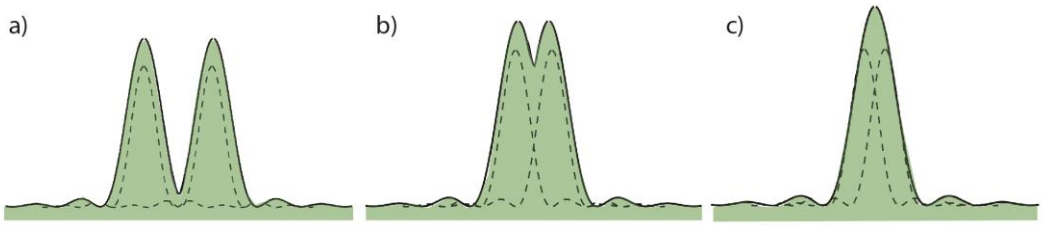

Figure 1.2 Rayleigh criterion.

This is the generally accepted criterion for determining the resolution of the imaging process and is called the Rayleigh criterion[2]. Practically, by assuming that the NA is ~1.3 for high quality objectives available, the equation (1.1) can be simplified to

$$d = \frac{\lambda}{2} \tag{1.2}$$

where λ is the wavelength of light used. Therefore, according to equation (1.2) for visible light, the spatial resolution limits to the range ~200 – 350 nm; in order to improve the resolution, light

with shorter wavelengths towards the UV region needs to be used. This gives rise to practical problems, for example in biological studies where exposure to UV could destroy the sample under investigation. Also, in order for imaging and spectroscopic studies of single molecules and viruses, the resolution needs to be improved down <10 nanometers. This level of resolution could never be achieved with diffraction limited optical systems. In other words, confinement of light down to this scale is not realistic with conventional optics, and a new approach was needed for light confinements at the nanometer scale.

1.2 Aperture type Scanning Near-field Optical Microscopy (Aperture SNOM)

The Equation (1.1) clearly states that *d* is directly proportional to λ and inversely proportional to NA. Also, as discussed above, there are significant limitations of using shorter wavelengths. These limitations compelled scientists to explore alternative ways of achieving higher resolution in optical instruments. In the early 20th century, Edward Synge proposed a new type of optical microscope that uses a tiny orifice in an opaque metal film, that is capable of overcoming the constraints imposed by the diffraction limit[3]. As Synge proposed, in this method

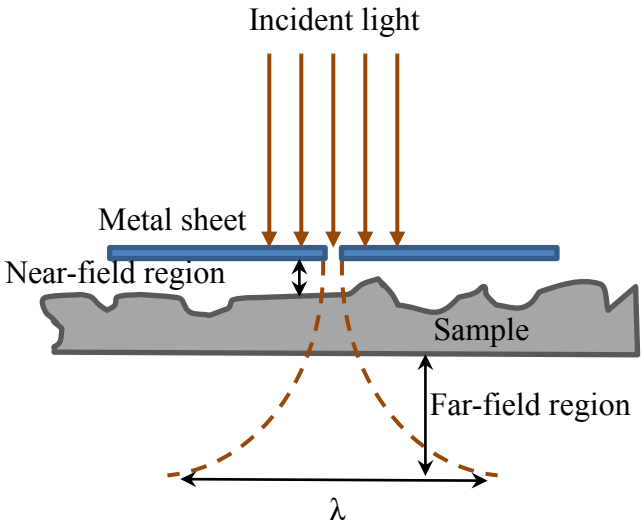

Figure 1.3 Schematic of the method proposed by Synge to beat the diffraction limit. Light is passed onto the sample surface through a subwavelength size aparture in the metal sheet.

the resolution is independent of the wavelength; instead it depends on the size of the aperture. This

idea was first experimentally realized by Ash and Nicholls about four decades after Synge proposed it; they achieved λ/60 resolution using microwave radiation of λ= 3 cm shining on a metal grating[4].

Using this technique with shorter wavelengths in the visible region was still challenging due to the practical difficulties in making smaller apertures and sample manipulations in smaller lengths. However, the results obtained by Ash and Nicholls fascinated the scientific community who were working in the same field and motivated improving the technique slowly but steadily. This laid the foundation for aperture type scanning near-field optical microscopy (SNOM).

Aperture SNOM was developed as an optical microscopic technique that breaks the far field resolution limit. In order to do that, this technique exploits the properties of a special type of waves that are called evanescent waves or evanescent field[5] associated with the light in the near-field region shown in Figure 1.3. Instead of an aperture in a metal sheet, Aperture SNOM deploys a tapered probe, a small metal aperture at the dielectric fiber tip with an additional thin metal coating to enhance the optical sensitivity. When the aperture probe is in close proximity to the sample

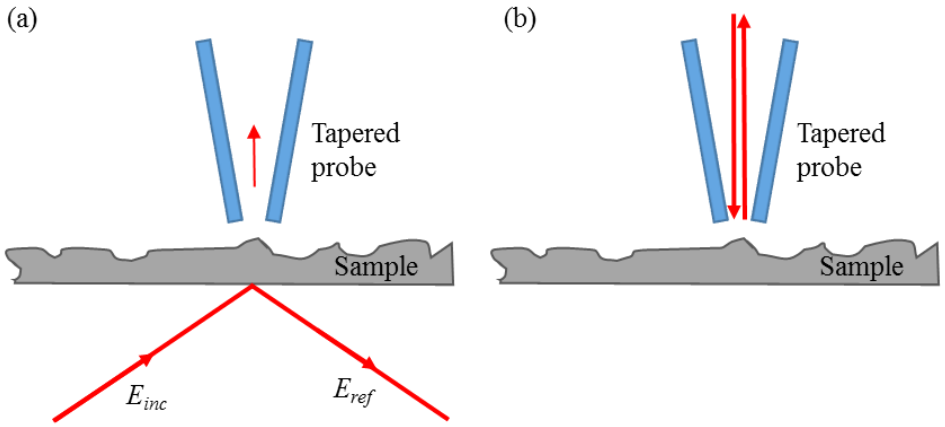

Figure 1.4 Two of several different configurations of aperture SNOM setup with (a) far-field illumination and near-field detection, and (b) illumination and detection both are near-field.

surface, a small part of the near field couples with the probe through the aperture. As explained before, the resolution of aperture SNOM primarily depends on the aperture diameter, d. However,

aperture probes are difficult to use at mid-infrared wavelengths. This is because of a cut-off effect that is experienced in the metal-coated fibers for diameters smaller than the wavelengths. For example, at a wavelength of 10 μm, the transmission through a 100 nm diameter aperture is reduced to the very small part of 10^{-25} of the incident intensity[6].

2 SCATTERING TYPE SCANNING NEAR-FIELD OPTICAL MICROSCOPY (s-SNOM)

The scattering type scanning near-field optical microscopy (s-SNOM) setup is typically developed based on a cantilevered tip of an atomic force microscope (AFM). AFM is a well-known member of the scanning probe microscopes (SPM) family. Different varieties of AFMs are designed to obtain images and measure local properties, such as height, friction or magnetism at nano-scale resolution. It generates surface images by raster-scanning the probe over an area of interest on the sample. There are three different basic operation modes for AFMs: Contact mode, Non-contact mode, and Tapping mode. In contact mode, also known as static mode, the tip scans the sample in close contact with the surface. The other two modes are called dynamic modes as the as the cantilever and tip vertically oscillate at a certain frequency during scanning process. In

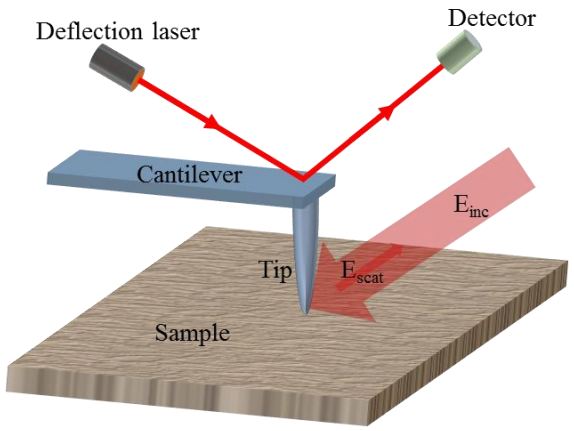

Figure 2.1 A typical s-SNOM configuration based on AFM.

non-contact mode, the tip is scanned above the sample surface at a distance ~ 5- 15 nm. Attractive Van der Waals forces acting between the tip and the sample are detected, and topographic images are constructed by scanning the tip above the surface. A schematic of the tip-cantilever-sample with illumination laser and deflection laser are shown in Figure 2.1. The vertical bending (deflection) of the cantilever due to forces acting between the tip and sample surface is detected by a laser (deflection laser) focused on the back of the cantilever. The laser is then reflected by the

cantilever onto a sensitive photodetector at a distant position. The position of the laser spot that falls on the photodetector provides a well correlated measurement of the movement of the probe tip relative to the sample surface. In order to assure the highest degree of precision of the movements, the probe is moved over the sample by a scanner that uses a piezoelectric. Probe tips that are made of Si or Si based semiconductors such as SiO_2 or Si_3N_4 are commonly used for typical AFM experiments. The radius of typically used probe tips ranges from ~5 to 50 nm. However, for near-field experiments, sharp probe tips with metal coating are used in order to enhance the near-field optical interaction between tip and sample surface. For near-field experiments, a cantilevered probe tip operated at tapping mode is illuminated by a focused laser beam with the desired wavelength. With the illuminated laser beam, the tip functions as an antenna converting the illuminating radiation into a highly localized and enhanced near field at the tip apex. The scattered radiation by the tip-sample coupled system is modified in both its amplitude and its phase due to the near-field interaction between the tip and sample depending on the local dielectric properties of the sample. Interferometric detection of the backscattered light thus yields nanoscale-resolved amplitude and phase images, rendering the local, complex dielectric function of the sample.

For all near-field experiments reported in this work, custom built commercial reflection mode s-SNOM system from Neaspec GmbH (neaspec.com) has been used with metal coated cantilevered probe tips from NanoWorld AG (nanoworld.com). The coating consists of a platinum-iridium layer deposited on both sides of the cantilever. The tip side coating enhances the conductivity of the tip and allows electrical contacts. The detector side coating enhances the reflectance of the laser beam and prevents light from interfering within the cantilever. The radius of these tips are typically <25 nm and the height ranges from 10 to 15 μm. The average dimensions

of the cantilevers are 160 µm (length) x 45 µm (width) x 4.6 µm (thickness); the average force constant is about 42 N/m and the average resonance frequency is about 285 kHz.

2.1 Theoretical Basis of s-SNOM

In 1996, proving that the resolution of the scattering type SNOM depends on the probe tip radius, but not on the wavelength used, Boccara *et al*[7] achieved a spatial resolution of 17 nm using a tungsten probe with the tip radius <20 nm. They used IR radiation of λ = 10.6 µm generated by a CO_2 laser; so the resolution achieved was ~ $\lambda/600$.

Nonetheless, the origin of the optical near-field image contrast was still a complex puzzle to be solved since the observed contrast is the contribution from different optical interactions namely scattering, reflection and absorption of electromagnetic radiation. Moreover, it showed a strong dependence on the optical dielectric constant of the sample material[8] and the topographic nature of the sample surface. In 1999, Knoll and Keilmann suggested a radically different model to explain this phenomenon[9].

2.1.1 Dipole Model

As shown in Figure 2.2, they modelled the light scattering by considering the electrical dipole moment of the tip together with its mirror image formed in the sample. In order to simplify the calculations the tip was approximated as a sphere, and the metal cone that right above the sphere has not been considered in this model[9]. By assuming the metallic tip as a polarizable sphere with radius a ($<< \lambda$) and dielectric constant ε_t, the polarization of the sphere can be expressed as

$$p = \alpha E_{inc} \tag{2.1}$$

Where α is the polarizability of the sphere andcan be given as

$$\alpha = 4\pi a^3 \frac{\varepsilon_t - 1}{\varepsilon_t + 2}. \tag{2.2}$$

In the presence of an incident field E_{inc}, the antenna action of the tip's shaft leads to an enhanced near-field that suggests the dipole induced by E_{inc} can only point in the direction of tip's

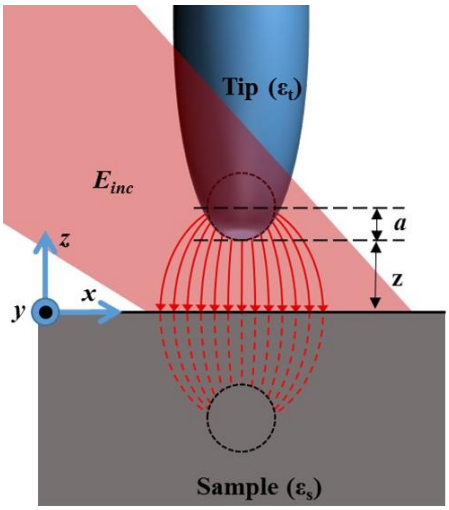

Figure 2.2 Dipole model of near-field interaction between tip and sample surface.

axis. For convenience, the tip axis is taken as *z*-axis and the sample surface boundary is taken as the *x*-*y* plane. Accordingly, the sample fills the half-space $z < 0$. The polarization of the mirror diploe created can be expressed as

$$p' = \beta p \tag{2.3}$$

The polarizability of the mirror dipole, β, in the sample can be written as

$$\beta = \frac{\varepsilon_s - 1}{\varepsilon_s + 1}. \tag{2.4}$$

Using electrostatic approximation the field that the mirror dipole generates at the tip dipole, E′ can be given by

$$E' = \frac{p'}{2\pi(2(z+a))^3}. \tag{2.5}$$

Then the dipole moment of the tip dipole can be modified as

$$p = \alpha(E_{inc} + E') = \alpha\left(E_{inc} + \frac{p'}{2\pi(2(z+a))^3}\right). \tag{2.6}$$

Hence, by using *(2.1)* and *(2.6)*,

$$p = \frac{\alpha}{1 - \frac{\alpha\beta}{2\pi(2(z+a))^3}} E_{inc} = \alpha_{eff} E_{inc}. \tag{2.7}$$

where α_{eff} is defined as the effective polarizability for the tip-sample system with

$$\alpha_{eff} = \frac{\alpha(1+\beta)}{1 - \frac{\alpha\beta}{16\pi(z+a)^3}}. \tag{2.8}$$

where z is the distance between the end of the tip and the sample surface. Importantly, all α, β, ε_t and ε_s are quantities with imaginary components in general. When $z \ll \lambda$, the scattering cross-section, C_{sca} is much smaller than the absorption cross-section, C_{abs} where $C_{abs} \propto Im(\alpha_{eff})$ Hence the scattered field, $E_{sca} \propto \alpha_{eff} E_{inc}$ and this implies that the coupled dipole system as well is complex valued and can be written as

$$\alpha_{eff} = \mathfrak{s} e^{i\varphi}, \tag{2.9}$$

where $\mathfrak{s}$ is the relative amplitude and φ is the phase shift between incident and scattered light.[10] This necessarily implies that contrast in the near-field image reflects the dielectric contrast of the materials in the sample.[10]

2.1.2 Finite Dipole Model

The Finite diploe model is a further improved model to overcome the limitations of the simple dipole model discussed in section 2.1.1. In this model, the tip is approximated more realistically by a spheroid with length 2L, instead of a sphere. The electric field field in the proximity of such a spheroid can be described by an extended or finite dipole, rather than a point-dipole. At large distances from the tip, the electric field of the spheroid converges to that of a point-dipole again. Eventually, the effective polarizability, α_{eff} can be expressed as a function of *z, β, a, L* and a complex constant that represents the total charge induced in the spheroid.

2.1.3 Extended Finite Dipole Model

This is a model specifically developed for extracting the phase and amplitude signals from experiments of single-particles on a substrate that is mostly useful in analyzing small structures such as viruses, molecules and nanoparticles. The main assumption in this model is that the radius of the particle of interest, *r* is smaller than the probe tip radius, *a*. The coupling between the combined system of sample, tip, and substrate are all taken in to account in calculating the α_{eff} modelling by spheroid, sphere and the semi-infinite half-space, respectively.

2.1.4 Theoretical and Computational modeling of Nano-scale Tip-Sample Interaction

Another advanced model has been proposed by Y. Abate et al, in the chapter "*Towards Understanding and Control of Nanoscale Phase Segregation in InGaN Alloys*" in the book "*III-Nitride Materials and Nano-Structures*" edited by Z. C. Feng for Imperial College Press (Currently in press). That proposed model is briefly explained in this section.

Unlike earlier models such as semi-analytical point-dipole[11] or finite-dipole approximations, this novel model relies on evaluation of the tip-sample polarizability numerically

using the frequency-domain solver of CST Microwave Studio. Thus, the tip-sample near-field interaction is completely taken in to account, and this model is capable of dealing with thin films as well as nanoparticle samples without using any fitting parameters.

The optical interaction between the tip and the sample is extremely complicated when a tip is placed close to a sample surface and illuminated by a laser beam. Due to the electric field enhanced by the tip, localized oscillating surface charges are induced in the sample. These oscillating surface charges, in return, induce charges at the tip surface. The outcomes of the tip-sample interactions can be well approximated by an effective dipole moment, $d_{\mathrm{eff}}(t)$, since these interactions are only efficient over distance much smaller than the wavelength of the incident light. The field radiated by $d_{\mathrm{eff}}(t)$ is the scattered light that depends on geometric and compositional properties of the tip, sample properties, and the tip-sample distance. This scattered light is interferometrically measured by mixing it with a reference beam in the s-SNOM system.

It is crucial to suppress contributions from other kinds of scattering such as scattering at surface roughness and scattering by the tip shank, that do not involve the near-field tip-sample interaction. This is achieved by utilizing a homodyne detection scheme. First, the tip vertically oscillates with a frequency of $f_{\mathrm{T}} = 2\pi\omega_{\mathrm{T}}$, which is typically about 300 kHz. When the distance between the sample surface and the tip apex is small (2-50 nm), the light is highly concentrated between them, so that the scattered field strongly depends on the size of the tip-sample gap. Then, the reference beam is modulated by making a mirror vibrate with a frequency, $f_{\mathrm{M}}(= 2\pi\omega_{\mathrm{M}})$ which is typically 300 Hz. The electric field of the signal, $E_{\mathrm{S}}(t)$ and that of the reference beams, $E_{\mathrm{M}}(t)$ are combined at the beam splitter and directed to the detector. The detector signal which is proportional to $|E_{\mathrm{S}}(t) + E_{\mathrm{M}}(t)|^2$ is then Fourier transformed and analyzed.

A theoretical approach was developed to numerically construct the s-SNOM images based on the near-field contrast variations by taking the height of the particles, and compositional dependent dielectric constants in to account. The effective polarizability of the tip-sample system, $\alpha_{\text{eff}}(h)$ is evaluated using height-dependent reflectivity, $r^{(\text{CST})}(h)$ calculated by the CST solver:

$$\alpha_{\text{eff}}(h) = ia_1a_2\left(r^{(\text{CST})}(h)\right)^* e^{-2ik_0\cos(\theta)(z_{\max}-z_{\text{pos}})}/(2\pi\, k_0 \tan\theta) \tag{2.10}$$

where, a_1 and a_2 are the dimensions of the simulation box along the x- and y-axes, respectively, k_0 is the wave vector of the incident beam, and θ is the angle of incidence, z_{max} is the upper boundary of the simulation box, and z_{pos} is the coordinate of the substrate surface.

The effective polarizability obtained in *Equation 2.10* is then used to calculate the far-field radiation given by

$$E_S(h_0 + \Delta h \sin\omega_{\text{T}}t) = \sum_n s_n e^{in\omega_{\text{T}}t} \tag{2.11}$$

where s_n is the amplitude of the complex s-SNOM signal, *n* is the demodulation order, and ω_{T} is the natural frequency of the probe tip. By combining E_{S} with a reference field E_{M} that is reflected from an oscillating mirror, a pseudoheterodyne interferometer scheme is implemented to simulate the real s-SNOM experiment. The normalized amplitude of s-SNOM signal is extracted by dividing the signal at the sample by that at the substrate: $(A_{\text{norm}})_n = \frac{|s_n(\text{sample})|}{|s_n(\text{substrate})|}$. The normalized amplitude signal is then numerically demodulated to compare with the experimental results.

2.2 Background Elimination through High Harmonic Demodulation

One of the major issues to deal within scattering type SNOM is the background scattering contribution from the detector signal.[15] This background scattering is caused by illumination using a micrometer sized laser spot that is focused using regular optical lenses. Even though the prime

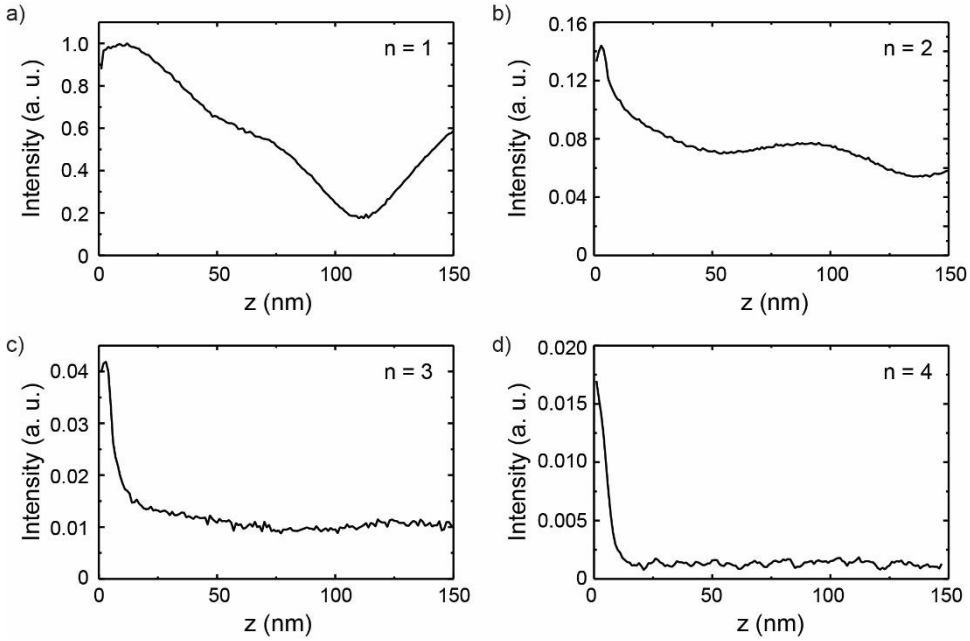

Figure 2.3 s-SNOM amplitude signal as a function of tip-sample distance, z for demodulation order n = 1-4 obtained for a Si sample using PtIr tip of radius ~ 20 nm with IR illumination of λ=10.2 μm.

goal is to illuminate the tip apex, a laser spot of micrometer size illuminates a significant area of the sample surface and a considerably larger part of the AFM probe shank as well. This results in generating unwanted scattering from these areas that is large enough to bury the relatively smaller near-field scattering in it. An early suggestion[15a] was made to have the probe and sample oscillate at two different, but closer frequencies in the direction normal and parallel to the surface respectively, while being illuminated by the laser.

This method enabled the detector to receive near-field signal at a difference frequency of the two aforementioned frequencies having a higher resolution with minimized background signal that suppresses the desired near-field signal.[15a] However, this method was not sufficient for a complete

suppression of the background signal.[15b] A rather improved approach to eliminate the background scattering is demodulation of the detector signal at higher harmonics nΩ (n≥ 2) of the tapping frequency, Ω of the tip.[16] However, in the process of image formation in this method, it maps the complex quantity $s_n e^{i\varphi_n}$ that is derived from $\alpha_{eff} = se^{i\varphi}$ instead of α_{eff} itself. Figure 2.3 illustrates the effect of demodulation of the s-SNOM amplitude signal; each plot demonstrates the dependence of the amplitude signal on the tip-sample distance. When *n* increases from 1 to 4, the amplitude signal drastically drops when moved away from the surface. At *n* = 4, amplitude signal intensity becomes almost zero within less than 25 nm away from the sample surface. The interface of a silicon surface and a PtIr probe with a tip of radius ~20 nm was illuminated with an IR laser of λ=10.2 μm. Signal intensity is plotted as a function of distance, z to the tip apex from the sample surface.

2.3 Interferometric Detection of the Near-field Signal

Different interferometric detection schemes are being used to achieve a cleaner near-field signal by eliminating the background scattering signal. Heterodyne interferometric detection technique is a method that is used to completely suppress the background signal.[16b, 17] As shown

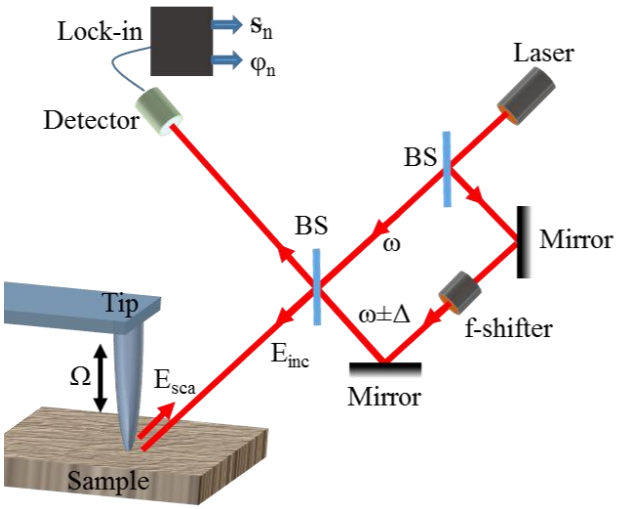

Figure 2.4 A heterodyne detection scheme utilized with s-SNOM

in Figure 2.4, in the heterodyne interferometric method, a frequency difference, Δ is introduced between the light used for tip illumination and the reference wave. The laser beam is split into two beams using the first beam splitter (BS); one beam goes directly to the second beam splitter while the other (reference) beam goes through a frequency shifter giving a frequency shift of ± Δ and then directed back to the second beam splitter. Then the output signal from the detector is sent to a lock-in amplifier and demodulated at a frequency Δ ± nΩ so that the amplitude, s_n and phase shift, φ_n can be separately extracted simultaneously. [21-22] An acousto-optic modulator (AOM) is usually used to generate the required frequency shift. However, in realizing this technique for different spectral regimes, there are several instrumentation limitations that and practical difficulties that must be addressed.[18]

In 2006, Ocelice and coworkers suggested an alternative "pseudoheterodyne" technique to overcome the practical difficulties faced in the heterodyne detection scheme discussed above.[18] This pseudoheterodyne technique has been previously utilized with aperture-SNOM coupled with a Mach-Zehnder interferometer.[19] In this method, a phase-modulated signal together with high harmonic demodulation was used instead of the frequency shifting used in the heterodyne method.

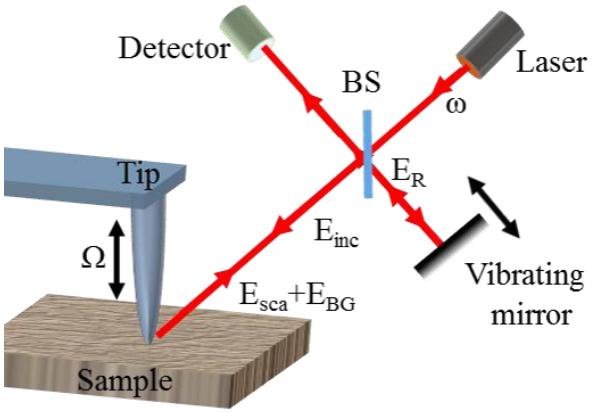

Figure 2.5 A Pseudoheterodyne detection scheme utilized with s-SNOM

As shown in Figure 2.5, a laser beam with frequency ω, emitted from the source is incident on the beam splitter, the reflected beam is then incident on the vibrating mirror and reflects back

(reference beam, E_R) to the detector through the beam splitter. The transmitted beam illuminates (E_{inc}) the tip-sample region; the scattered beam ($E_{sca} + E_{BG}$) from the tip-sample region that carries both near-field signal and background signal is then incident on the beam splitter and reflects to the detector. Compared to the heterodyne configuration that requires two beam splitters and AOM, this technique is relatively easier to implement because it only requires one beam splitter and a vibrating mirror in a Michelson interferometer configuration. Also, it does not have any spectral limitations imposed by AOM, so it can be used to cover a wider spectral window ranging from near-UV to far-IR.

2.4 S-SNOM Experimental setup

A s-SNOM experimental system basically consists of three main parts: illumination unit, AFM unit and detection unit. Figure 2.6 shows the schematics of a complete s-SNOM experimental setup with the components for illumination and detection. The laser beam emitted by

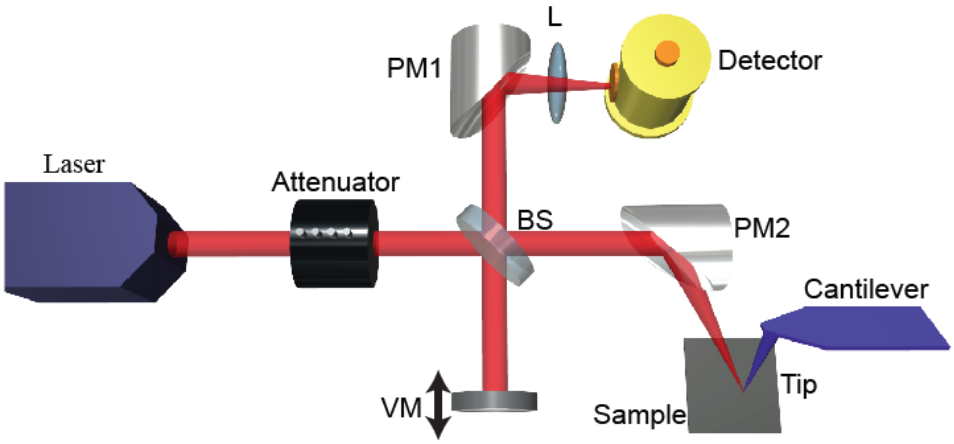

Figure 2.6 Schematics of s-SNOM experimental setup

the source is sent through a set of attenuating filters to get the required power level. Then this beam is incident on the beam splitter so that the reflected beam incident on the vibrating mirror (VM) and the transmitted beam is focused and directed to illuminate the tip-sample interface using a parabolic mirror (PM2). The scattered beam from the tip-sample system is directed back to the

beam splitter via the same optical path that is used to illuminate. Both the reference beam reflected from the vibrating mirror and the scattered beam incident on the beam splitter are then directed to the detector using a parabolic mirror (PM1) and a converging lens (L).

2.5 Nano- Fourier Transform Infra-Red (Nano-FTIR) Spectroscopy

Nano-FTIR is a spectroscopic technique that is based on the s-SNOM technique. We used the nano-FTIR module that was developed by Neaspec GmbH. Similar to the s-SNOM imaging system, this module employs a Michelson interferometer that uses a linearly moving reference mirror to illuminate the tip-sample system and detect the scattered signal from it. However, it uses a broadband source for illumination instead of single frequency laser. Together with the integrated broadband IR light source that covers from 5 to 15 μm from Toptica photonics AG, it enables IR spectroscopy with nanoscale spatial resolution on a wide range of samples including 2D materials, organic compounds, polymers, biological and other soft matter in ultra-small quantities.

3 PROBING STRUCTURAL CHANGES REQUIRED FOR MEMBRANE FUSION IN SINGLE ENVELOPED VIRUS PARTICLES

3.1 Introduction

Many viruses continue to be a persistent threat to human populations. To enter a cell, viruses attach to host-cell receptors. Detailed understanding of how viral entry proteins interact with their host-cell receptors and undergo conformational changes that lead to entry offer enormous opportunities for the development of novel therapeutics and vaccines. The surface hemagglutinin (HA) of influenza virus particles is anchored to the membrane envelope of the virus that is underlined by a layer of matrix protein M1[20]. The ribonucleoprotein complex (RNP) inside the virus particle is composed of the nucleoprotein (NP) and fragmented genomic RNAs. During infection, the virus particle is uptaken by endocytosis after binding the host receptor via HA. Following reduction of the luminal pH, that causes conformational changes in HA, membrane fusion begins in the endosome, which successively leads to entry and release of the viral genome[21].

We have used scattering type scanning near-field optical microscopy (s-SNOM) which allows direct diffraction unlimited experimental access to the nanoscale detailed structural and chemical as well as mechanical changes of a single influenza virus. s-SNOM provides nano-spectroscopy capability at spatial resolution down to ~10 nm in the IR fingerprint region (1800-900 cm^{-1}), for high resolution in situ spectroscopic mapping of a single virus and its interaction with environmental triggers[15c, 22].

This chapter is based on the article titled "Probing Structural Changes Required for Membrane Fusion in Single Enveloped Virus Particles Using Nano-Infrared Spectroscopic Imaging" by Sampath Gamage, Marquez Howard, Hiroki Makita, Brendan Cross, Gary Hastings, Ming Luo and Yohannes Abate. Submitted to the Journal of Virology.

3.2 Experimental Details

3.2.1 Specimen Preparation

To prepare the influenza virus, Madin-Darby canine kidney (MDCK) cells were maintained with EMEM media complemented with 4% fetal bovine serum. Confluent MDCK cells were infected with influenza A virus (STRAIN X-31) at a MOI of 1.0 in EMEM media containing 2 µg/mL TPCK-treated trypsin, and the infected cells were incubated at 37 °C, 5% CO_2. The media were collected after 48 hours post infection. After clarification to remove cell debris, the virus was pelleted through a 33% sucrose cushion at 85,000 x g. The virus pellet was re-suspended in PBS and pelleted again through a 30% glycerol cushion at 15,000 x g. The virus pellet was re-suspended in PBS and stored at 4 °C before usage. The virus particles are then drop casted on pre-cleaned Si wafer for s-SNOM experiments. After sitting for 15 min, unbound particles were washed off with water. For changes of condition, the particle deposited wafer was incubated with 1M HCl solution at various pH values, or 1 µM of compound 136 in 1% DMSO.

3.2.2 Far-field Fourier Transform Infta-Red (FTIR) Spectroscopy

Transmission type FTIR measurements were undertaken using a Varian 7000 FTIR spectrometer coupled to a Varian UMA600 IR microscope. Transmitted IR light was detected by a single element 0.25 mm^2 mercury cadmium telluride detector. FTIR data was collected in the 7000-100 cm^{-1} spectral region, although data is only presented in the 1800-950 cm^{-1} region. All FTIR data was recorded at 4 cm^{-1} spectral resolution. A few µL of all biological materials to be sampled were pipetted onto a 13 mm diameter zinc selenide window and allowed to air dry for ~ 1 hour prior to measurement. Spectra were obtained at several ~100x100 μm^2 spots on the pipetted samples. Spectra obtained at the different spots were averaged. Each spectrum is the average from ~640 interferograms.

3.2.3 s-SNOM Nanoimaging

The heights of the viruses were measured from the topography image. The near-field phase, being directly proportional to the imaginary part of the permittivity, represents vibrational absorption of a sample.[10, 15b, 15c, 23] The near-field spectra were obtained by measuring the normalized phase, $\Delta\varphi$ (phase difference between signal on top of a virus and background, $\Delta\varphi = \varphi_n(\omega)-\varphi_n(\omega)_{ref,n}$) at different frequencies.

3.3 Results and Discussion

As shown in Figure 3.1a, s-SNOM functions as a local probe via scattering of the nanolocalized optical fields from a probe tip either at single frequency or using broadband light sources covering a wide IR frequency range. It is well established that the near-field phase, being directly proportional to the imaginary part of the permittivity, represents vibrational absorption of a sample[15c, 23a, 23b]. Thus s-SNOM directly offers spectroscopic mapping of the vibrational

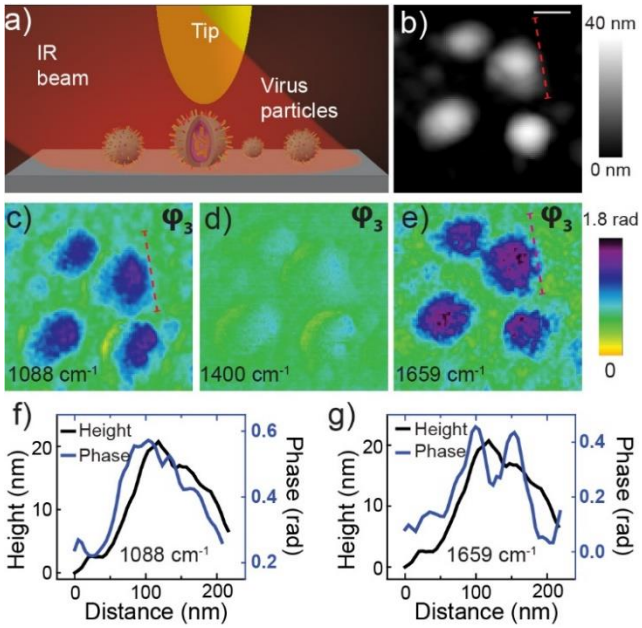

Figure 3.1. s-SNOM experimental setup and near-field infrared spectral images of influenza virus at pH 7.4. (a) s-SNOM experimental setup, (b) topography of four viruses (scale bar is 100 nm), (c-e) near-field phase (φ3) spectral images. Line profiles of topography and phase at 1088 cm^{-1} (f) and 1659 cm^{-1} (g)

fingerprints of a single virus at nanoscale spatial resolutions via this correlation[15b, 23c-e]. This capability of s-SNOM is demonstrated in Fig.1b-e. Fig. 1b shows a topography image of viruses with height in the range ~30-40 nm and diameter ~70-100 nm. Near-field phase (φ_3) images at

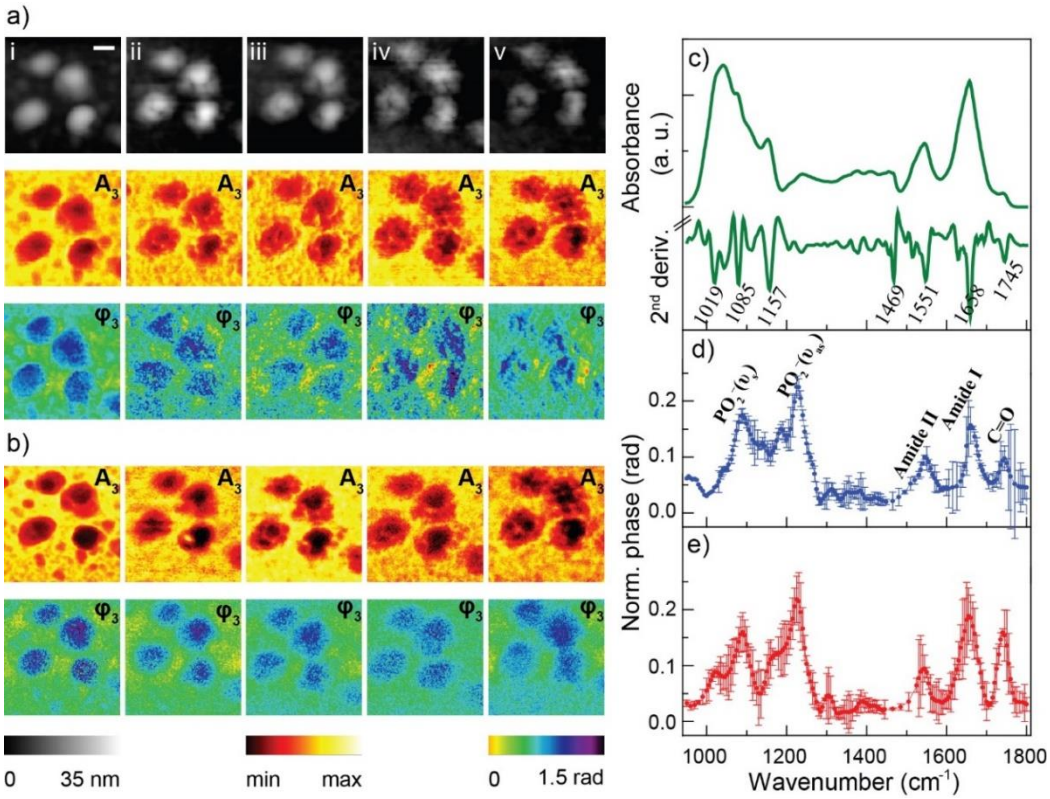

Figure 3.2 Spatial evolution of virus particles at progressively more acidic pH. Topography (black & white), scale bar 100 nm and near-field amplitude (A3) and phase (φ3) images of four virus particles at progressively lower pH (left to right). Spectral images taken at (a) 1088 and (b) 1659 cm^{-1}. Far-field FTIR spectrum and its second derivative of virus particles at neutral pH (c), near-field single virus IR spectrum at neutral pH (d) and at pH 5 (e). The columns i-v in the topography represent successively decreasing pH from neutral (i) to pH 2 (v).

three laser frequencies are shown in Fig. 1c-e. The strong phase contrast at 1088 and 1659 cm^{-1} indicate strong vibrational absorption bands of the virus at these frequencies. The weak phase contrast at 1400 cm^{-1} demonstrates weak absorption at this frequency. From these near-field phase images the chemical specific structural properties of a single virus can be assessed. Remarkably, the spectral image at 1659 cm^{-1} (Fig. 1e) and the corresponding line profile (Fig. 1g) show HA

aggregates protruding out from the surface of the virus envelope. These aggregates are not well resolved in the topography (Fig. 1b,g). The HA protein aggregates are missing in the phase image taken at 1088 cm^{-1}. This is because the protein absorbs at 1659 cm^{-1} but not at 1088 cm^{-1}. In this way these spectral images provide insight into not only the spatial structure, but also the chemical composition of the surface of the virus. As shown in Figure 3.3, the near-field amplitude images

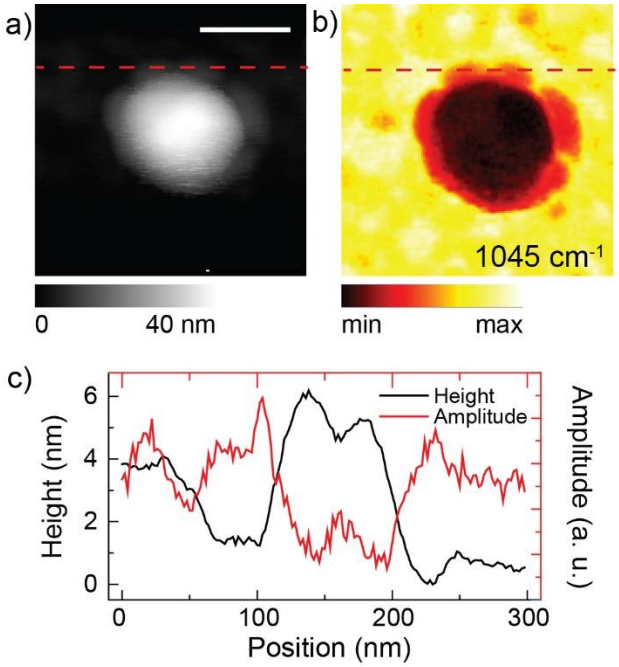

Figure 3.3 (a) Topography of a virus particle and (b) 3rd harmonic near-field amplitude image taken at 1045 cm-1 showing contrast difference between the outer viral envelop and the inner structure of the virus. (c) Topography and amplitude line profiles. Scale bar is 100 nm.

also can distinctly identify the viral envelop from the inner structure of the virus. However, detailed assignment of vibrational modes requires detailed spectra over a broad range, and it is to this issue that we now turn.

We first investigate the structural and spectral alterations in four virus particles as they are exposed to successively decreasing pH. Figs. 2a-b show s-SNOM topography images (black & white), near-field amplitude (A_3) and phase (φ_3) images taken at (a) 1088 and at (b) 1659 cm^{-1}. Images in columns (i-v) are obtained at successively decreasing pH from neutral (i) to pH 2 (v).

Surprisingly, both the near-field spectral and the topography images show that as the viruses were exposed to increasing acidity they start to break at a few locations, visible from the edges towards the middle (ii and iii, Fig. 2a). The breakage progresses at multiple locations as the pH is further decreased and eventually the whole structure is fractured. The 1659 cm^{-1} image, which represents the amide I protein absorption (spectral assignments are discussed in detail below), shows a uniform protein distribution across the surface of the viruses. In contrast, the 1088 cm^{-1} image, that represents phosphate absorption, is fragmented, more and more so at lower pH. These differences in the 1659 and 1088 cm^{-1} images likely indicate disintegration of the lipid bilayer as well as RNA at low pH. This direct visualization of the effect of low pH on single virus particles clearly demonstrates viral membrane breaking in the absence of a host cell membrane. This observation offers new insight into our current understanding of viral fusion.

In order to connect the nano- and microscopic realms, and also to aid in spectral band assignments, near-field and far-field IR spectra for influenza virus particles are compared in Figure 3.2. The far-field IR spectrum (Figure 3.2c) is for an ensemble of virus particles at neutral pH. The second derivative spectrum indicates precise frequencies of the many underlying bands that contribute to the IR spectrum. The near-field IR spectra are taken on several single virus particles, and the average spectra (including error bars) are plotted at neutral pH (Figure 3.2d) and after exposure to acidic solution at pH 5 (Figure 3.2e). The near and far field IR spectra share many similarities, especially in terms of peak positions. Band intensity ratios may vary somewhat, but this is expected for spectroscopic techniques that probe on very different length scales. To the best of our knowledge, these are the first far and near-field IR spectra ever reported for influenza virus particles. Many of the peaks in the far field IR spectra are well documented (see below) and, given the similarity of the far and near-field IR spectra, we can assign the bands in the spectra of single

virus particles, at both neutral and low pH. In the IR spectra, the broad bands centered near 1658 and 1551 cm^{-1} are the well-known amide I and amide II absorption bands, respectively. These bands are predominantly due to the HA proteins. The second derivative spectrum indicates shoulders in the amide I and II bands at 1629 and 1515 cm^{-1}, respectively. These bands may represent different protein secondary structures[24], or possibly contributions from multiple types of proteins. Amide I absorption at ~1629 cm^{-1} is often associated with β-sheet types of protein secondary structure[24]. In the amide I and II regions, the near field IR spectra both before (Fig. 2d) and after (Fig. 2e) acid exposure are quite similar. This observation is in keeping with the data in Fig. 2b, which also show similar phase images at 1659 cm^{-1} both before and after acid treatment. The amide I band appears somewhat broader after acid treatment which may indicate some, not unexpected, protein degradation (of HA, M1, and NP proteins) upon treatment.

The lipids of the influenza virus are the outer 4 nm thick membrane envelope in which spikes of the HA proteins are inserted[25]. The lipid membrane forms a key structural component of the virion providing an extraordinary biophysical stability to viruses, and are associated directly

with their infectivity. The peak centered near 1745 cm^{-1} in the IR spectra is well known to be associated with membrane lipids[26], in particular this peak is associated with lipid ester C=O absorption. Although this lipid C=O ester carbonyl absorption spectral region is free of other

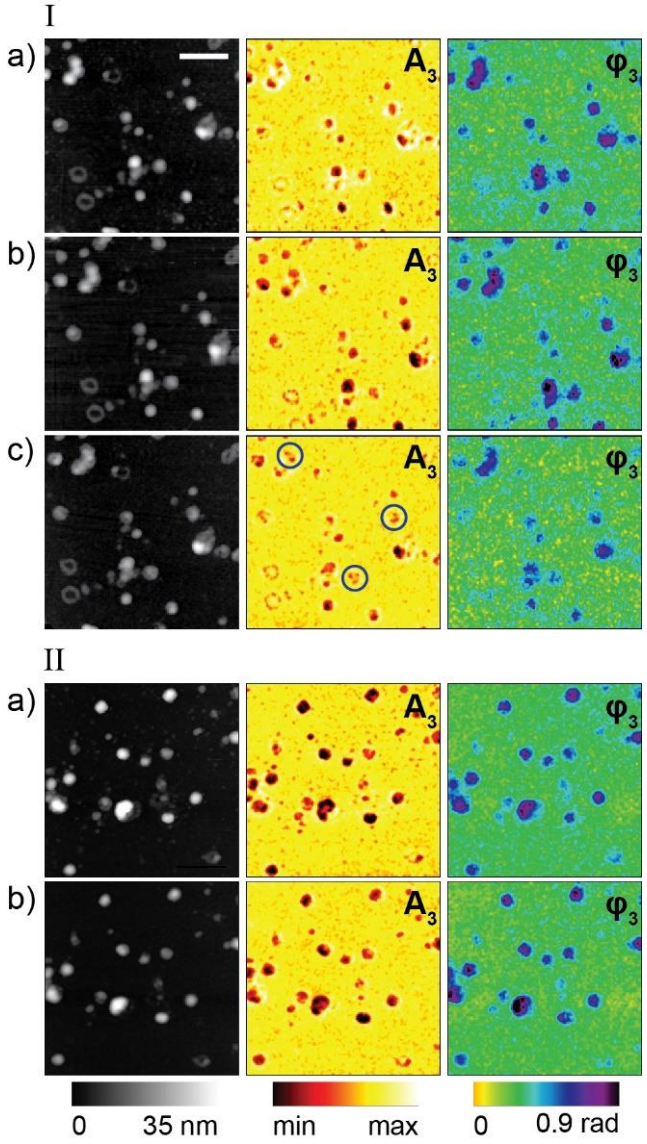

Figure 3.4 Topography, near-field amplitude and phase infrared images of several influenza virus particles i-(a), after compound 136 interaction (15 min) i-(b), followed by acid exposure i-(c). ii-(a-b) shows a different set of virus particles at neutral pH ii-(a) and ii-(b) shows the particles after acid exposure following compound 136 incubation (1 hr.). Scale bar in i-(a) is 100 nm.

significant infrared-active modes, the exact peak position and bandwidth can vary from virus to virus based on the thermal history of the sample and the way in which the sample is prepared[27].

On the other hand, our ability to identify lipid ester C=O bands on a single virus is very useful since contour modification of the band can be related to structural modifications, hydration of the bilayer interface and the polarity and other properties of the local environment[28]. Comparison of the near-field IR spectra in Figure 3.2d and Figure 3.2e indicates that while the ester C=O peak position is similar, the intensity of the peak is increased in the near field spectrum after acid exposure, this acid induced increase in lipid ester absorption is also observed in far-field spectra (Figure 3.5). The acid treatment obviously disrupts the membrane, providing greater exposure of membrane lipids to the probe tip.

In both the near and far-field IR spectra in Fig. 2, a broad set of features spanning the 1250-

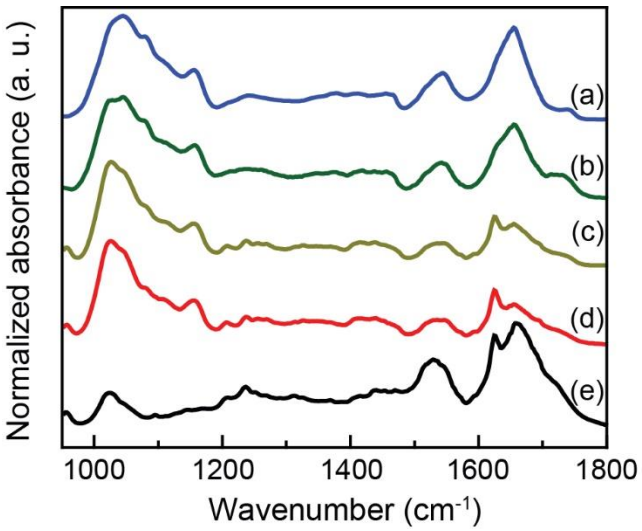

Figure 3.5 Far-field FTIR spectra. (a) Influenza untreated. (b) Influenza after exposure to acid treatment (pH 2). (c) Influenza after exposure to compound 136. (d) Influenza virus particles after exposure to compound 136 followed by acid treatment (pH 2). (e) Compound 136. Each spectrum is normalized to 1 and vertically shifted for clarity.

950 cm^{-1} region are observed, with the overall intensity of this set of features being larger than the amide I absorption band. It is interesting to compare this observation to IR spectra of whole cells[26], which generally display an amide I absorption band that is considerably more intense than absorption features in the 1250-950 cm^{-1} region. Since the bands in the 1250-950 cm^{-1} region are

associated mainly with RNA/lipids this implies that the ratio of RNA/lipids to protein derived from the IR spectra is higher in influenza virus compared to that found in other biological cell types.

Lipids[29], carbohydrates[30] and RNA[31] all display absorption bands in the 950-1250 cm^{-1} region[32]. As a result, this spectral range provides specific signatures of the lipid bilayer and RNA which offers direct information on their chemical and structural modification of enveloped viruses

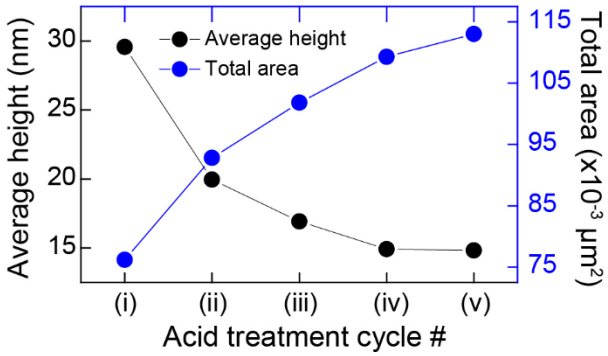

Figure 3.6 Geometric changes of virus particles due to acid treatments. Height (black points) and surface area (blue points), evolution plot of influenza x-31 virus particles as a function of decreasing pH from neutral (i) to pH 2 (v).

as the surrounding environmental pH is varied. Antisymmetric and symmetric phosphate (PO_2^-) stretching vibrations are known to occur near 1230 and 1085 cm^{-1} respectively. Bands near these frequencies dominate the near-field IR spectrum, and can also be distinguished in the far-field IR spectrum. It is likely that the bands at 1225 and 1088 cm^{-1} in the near-field IR spectrum are due to antisymmetric and symmetric phosphate vibrations of the lipid bilayer of the virus, respectively. We note that the RNA (PO_2^-) asymmetric and symmetric stretching vibration could also contribute to the broad peaks centered at 1225 cm^{-1} and 1088 cm^{-1}, respectively[33]. For both HCl treated and untreated viruses in both the far and near-field spectra, it is difficult to disentangle the relative contribution of the lipid and RNA as well as other biomaterials. Simultaneously with spectroscopic information, s-SNOM also provides assessment of geometric changes of single virus particles either due to successively lower environmental pH or thermal/mechanical changes. As shown in

Figure 3.6, the virus particles in general decrease in height and increase in surface area at low pH. In some cases, closely spaced virus particles can also deform and release the viral genome as shown in the time series images in Figure 3.7.

Recently, an antiviral compound (compound 136) has been reported that inhibits influenza virus fusion at picomolar concentrations in plaque reduction assays[34]. Compound 136 was found

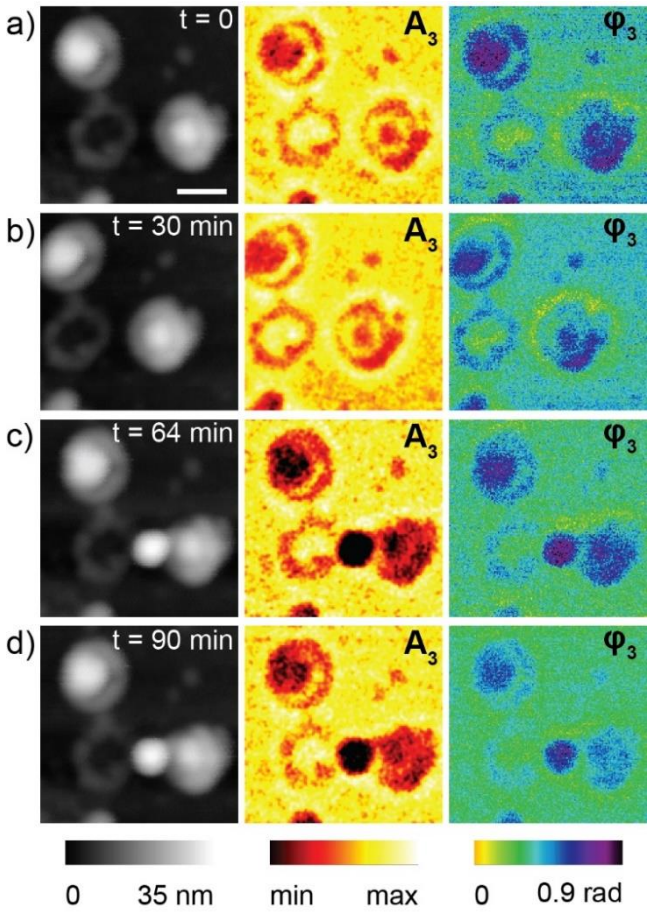

Figure 3.7 Deformation and release of the viral genome in closely spaced viruses imaged as a function of time using s-SNOM. Topography (black and white), 3rd harmonic near-field amplitude (A_3), and phase (φ_3) images of virus particles on mica. Scale bar is 100 nm.

to tightly bind to the viral envelope modifying its chemical signature and inhibiting influenza virus entry. Using our single virus particle imaging technique, we have characterized for the first time the effectiveness of this antiviral compound in stopping viral breakage during treatment with

low pH solutions. This is achieved by following the same set of single viruses incubated with compound 136 and further exposed to low pH. In Figure 3.4 we show topography, near-field amplitudes and phase images (taken at 1080 cm^{-1}) of the same set of viruses before applying compound 136 and neutral pH values (Figure 3.4-I-a), after incubation with 1 µM of compound 136 for 15 min (Figure 3.4-I-b) and then exposed to very high acidic solution (pH=2, 15 min) (Figure 3.4-I-c). Figure 3.4-II shows a different set of virus particles at neutral pH (Figure 3.4-II-a) the same set of particles after acid exposure following compound 136 incubation for 1 hr. is shown in Figure 3.4-II-b.

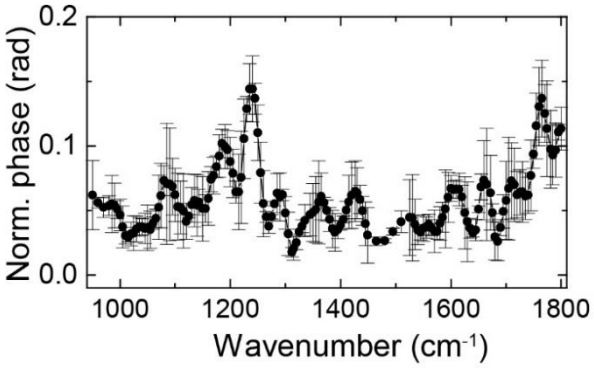

Figure 3.8 Nano-IR spectrum of compound 136 bound virus particles. Near-field IR spectrum (φ3) of virus particles incubated with compound 136 and treated by acid treatment (pH 2).

Careful examination of all the virus particles after incubation with compound 136 show that only 3 virus particles (indicated by black circles in Figure 3.4-I-c) out of ~25 particles broke while others remained intact when they were exposed to low pH solution. We then increased the time of the virus incubation with 1 µM of compound 136 (to 1 hr) and exposed the particles to the same pH solution as before. The results in Figure 3.4-II-(a,b) show that all the particles remained unbroken after low pH exposure confirming the effectiveness of compound 136 against viral membrane breakage induced by low pH.

3.4 Summary and Conclusion

In this work, we have undertaken spectroscopy and imaging experiments on single influenza virus particles in order to investigate the chemical and structural modifications of the viral protein and lipid bilayer during various environmental pH variations and upon interaction with antiviral compounds. A remarkable finding of our work is that we directly show that if the environment pH is lowered, breakage of viral membrane could occur without the presence of a targeting membrane, contrary to the current viral fusion model, which requires virus binding to a host cell membrane for forming the fusion pore to release the viral genome[35]. The fusion inhibitor compound 136 can effectively prevent the membrane breakage induced by low pH. Our results are likely to be applicable to other enveloped viruses and may open unique opportunities for fundamental virology studies not offered by traditional ensemble methods.

4 NANO-IMAGING AND SPECTROSCOPY OF EXFOLIABLE MATERIALS

4.1 Nanoscopy of Black Phosphorus Degradation

Mechanically exfoliable two-dimensional (2D) layered materials started becoming popular among the material scientists since the exfoliation of graphene in 2004. Many new materials are being added to this family, making it the most sought-after family of materials for both experimental and theoretical research. However, graphene, the material that laid the foundation for this new area of research has a very fundamental drawback in using it for device applications

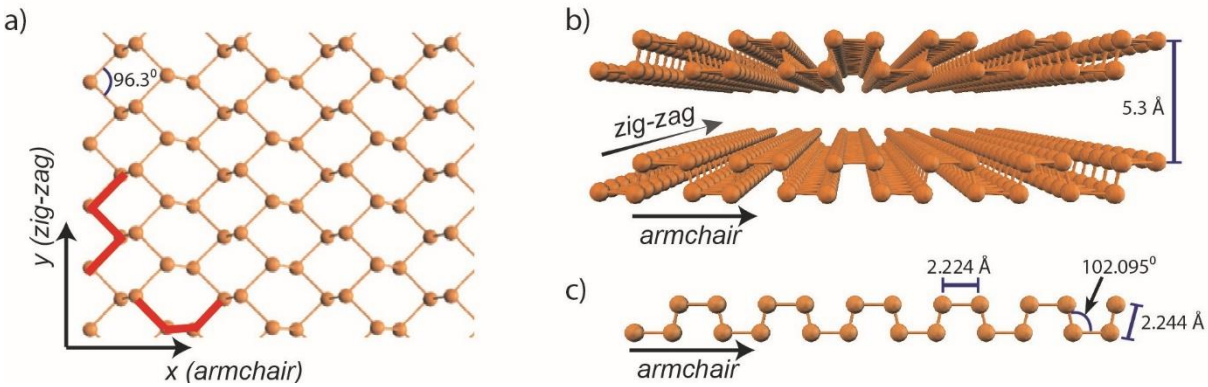

Figure 4.1 Atomic arrangement of orthorhombic black phosphorus layers. Top view (a) and side view in armchair direction (b) and (c).

because it does not have a natural energy band gap. Black phosphorus (BP) with three different crystalline structures−orthorhombic, simple cubic and rhombohedral[36] −is a mono-elemental 2D material that has joined this family. The orthorhombic BP, being that its semiconducting structure is of great interest due to its direct bandgap that exhibits when thinned down to several monolayers; these single layers of BP is known as phosphorene. Moreover, being that phosphorus atoms are the only constituent element of BP, it possess several other unique properties that graphene does not have. The in-plane phosphorus atoms are strongly bonded forming the layered nature of BP while the adjacent layers are weakly connected through van der Waals forces enabling it to be

mechanically exfoliable. As shown in Figure 4.1a, the atomic arrangement of BP exhibits two different directions within the BP lattice that leads to in-plane anisotropy. The direction parallel to the atomic valleys is named zig-zag direction and the direction perpendicular to the valleys is named armchair direction. In each monolayer, shows the puckered orthorhombic honeycomb lattice structure that phosphorus atoms connected with two types of P −P bond as shown in Figure 4.1c s. The separation of the nearest P atoms in the same plane is 0.2224 nm and the nearest atoms between the top and bottom of a monolayer are separated by 0.2244 nm.[37] Two adjacent

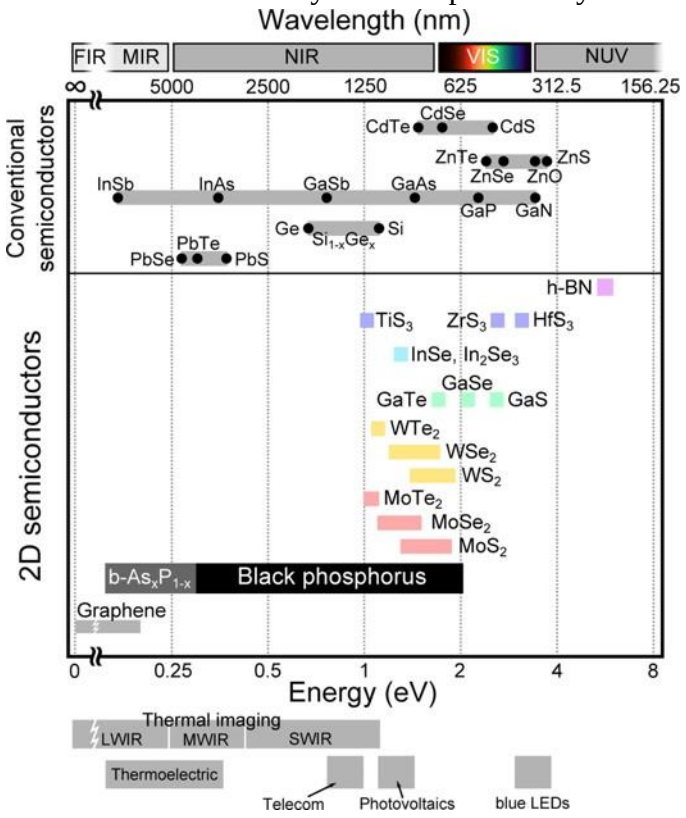

Figure 4.2 Black phosphorus: Bridging the gap between graphene and other 2D materials. Reprinted with permission from from ref. Copyright 2015 American Chemical Society.

monolayers are separated by 0.53 nm. In the z-direction, normal to the x-y plane it appears as a hexagonal structure with bond angles of 96.3° and 102.1°.[37-38] The significant structural anisotropy of BP discussed above leads to in-plane anisotropy in electrical and optical properties as well.

Having a direct bandgap is one of the crucial properties of a material to be used in the semiconductor industry. Most of the other 2D materials such as transition metal di-chalcogenides (TMDC) show a direct bandgap only for single layers. However, the bandgap of BP remains direct not only for a single layer but also for multiple layers; interestingly it is tunable by adjusting the number of layers used[36b, 39]. This thickness-dependent band gap is found to be due to stronger quantum confinement of the charge carriers in the out-of-plane direction compared to other 2D materials of interest. This thickness-dependent bandgap together with in-plain anisotropy and high carrier mobility, makes BP remarkable as a semiconductor material.[40] Specifically, this bandgap tunability of BP makes it an excellent candidate for bridging the gap between graphene and other 2D materials as shown in Figure 4.2.[41] Monoelemental BP covers the gap from ~2 eV (single layer) to 0.3 eV (bulk); moreover, when alloyed with arsenic it can be further tuned in the range from 0.15 to 0.3 eV so that it overlaps with the bandgap of graphene (0 - 0.2 eV) under certain specific conditions reported in literature.[42] Typically, TMDCs can be engineered to cover the bandgap ranging from 1.0 to 2.0 eV, hence BP has a good overlap with TMDCs in the higher gap range.

Similar to other 2-dimensional (2D) layered materials, BP can be prepared by simple mechanical exfoliation. The major impediment to research and prospective application of single/few-layer BP is its chemical degradation under ambient conditions[43].

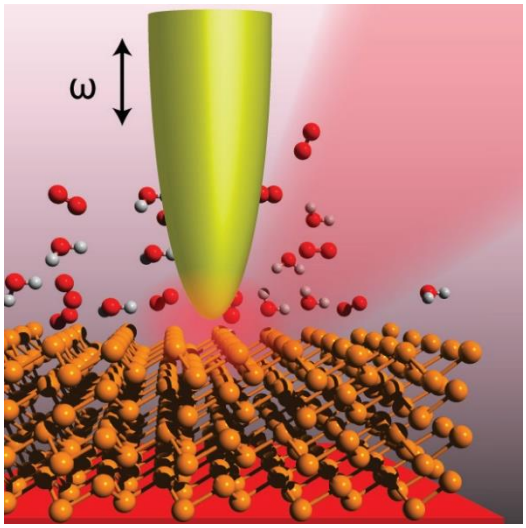

Figure 4.3 An illustration of few layer BP with AFM tip approached on the surface under ambient condition while red laser light shines the tip-surface interface.

An extensive understanding of the degradation process and reliable ways to achieve stable and scalable degradation protection is necessary in order to realize the full potential of this material in its single- and few-layer forms. Recent studies have shed light on the underlying mechanism and speed of degradation by AFM and spectroscopic techniques.[43-44] Few passivation methods have also been investigated with various degree of success to slow down and prevent degradation[45]. Breakthroughs in developing powerful passivation methods to overcome this degradation issue require deeper experimental understanding and theoretical modeling of the degradation process as well as the effectiveness of passivation techniques.

This chapter is primarily based on two journal publications[46] by the author after minor revisions and additions with permissions (please see Appendix B) from the publishers of the journals.

4.1.1 Study of Degradation Process

We report the first experimental quantification of geometric properties and theoretical modeling of the chemical degradation process of BP and investigate the effectiveness of

passivation coatings using infrared scattering type scanning near-field microscopy (s-SNOM)[47]. We chemically identify oxidized phosphorus species locally at the onset of degradation by nanoscale spectroscopic imaging at mid-infrared frequencies. We found that these species can form underneath 5 nm thick Al_2O_3 coating deposited by atomic layer deposition (ALD) indicating that thin coating is insufficient to protect BP against degradation caused by ambient medium. By performing simultaneous topographic and optical time series imaging over several months, we show that a nanolayer BP exposed to ambient environment degrades at a steadily increasing rate until saturation begins, so that the degraded area and volume of degraded regions as functions of time follow the well-known S-shaped growth curve (sigmoid growth curve)[48]. Phenomenological modeling of experimental results suggests a strong influence of degraded areas on adjacent BP. Our model is advantageous since it is based on elementary probabilities that can be related to the O_2 and H_2O content in the ambient medium, as well as to the chemical reaction processes that result in oxidized phosphorus species which allows, in principle, to predict the degradation time under different environmental conditions. Our work incorporates experimentally measured geometric patterns of BP degradation with model prediction allowing us to determine the growth saturation value, steepness of the growth and the mid-point of the growth, and the relative importance of neighboring interactions.

4.1.1.1 Experimental Details

Mechanical exfoliation was used for BP sample preparation on Si and SiO_2substrate. After the exfoliation, the substrates were loaded in to atomic layer deposition (ALD) chamber (Cambridge NanoTech, Savannah 200) immediately for the Al_2O_3 deposition with trimethyl aluminum (TMA) and water as precursors. For the first three rounds, only TMA is flowed through the chamber to prevent oxidization of the BP flakes. The ALD was performed at 200 °C. Various

thicknesses (1 nm, 5 nm, 10 nm, 20 nm, 50 nm and 100 nm) of Al_2O_3 were coated on the BP flakes using ALD. We performed infrared (IR) optical amplitude and phase resolved near-field spectroscopy imaging of unencapsulated BP flake left to degrade, in order to chemically identify the degraded regions in BP in the laser wavelength range, λ=5.5 μm−10.8 μm. We also performed a nano-spectroscopic study of an unencapsulated BP sample to extract the IR spectrum in the range of 800-1400 cm^{-1}.

4.1.1.2 Results and Discussion

Figure 4.4a shows the schematic of the s-SNOM imaging experiment Al_2O_3 coated BP flake. The topography image of a degraded region of a BP flake of thickness 10 nm together with the line profile is given in the Figure 4.4b. Simultaneously recorded IR third harmonic amplitude and phase optical images of the same BP flake are given in Figure 4.4c.

Although the various AFM height distributions shown in the topography and line profile images in Figure 4.4b are not sufficient to identify the chemical composition of nano-islands, taller topographic protrusions on BP samples exposed to ambient environment have been used to identify degraded regions[43]. The unique capability of s-SNOM is its ability to allow spectroscopic identification of islands at nanometer resolution regardless of the excitation wavelength[47-49]. Figure 4.4c shows third harmonic optical near field amplitude and phase images recorded simultaneously with topography at two laser wavelengths, 5.9 μm and 9.3 μm. In both amplitude

images, topographically higher BP nano-islands appear darker than the substrate. Such a negative contrast in the amplitude images is due to smaller dielectric constant of the darker island compared to the bright region as it is well known in s-SNOM imaging. The near-field amplitude contrast coupled with the observed topographic protrusions, indicate that taller islands have different material makeup due to ambient exposure. Further chemical identification is provided by the near-field phase images, which show a clear optical contrast difference between the images taken at the two wavelengths in Figure 4.4c. In the phase image taken at 9.3 μm we observe a clear contrast

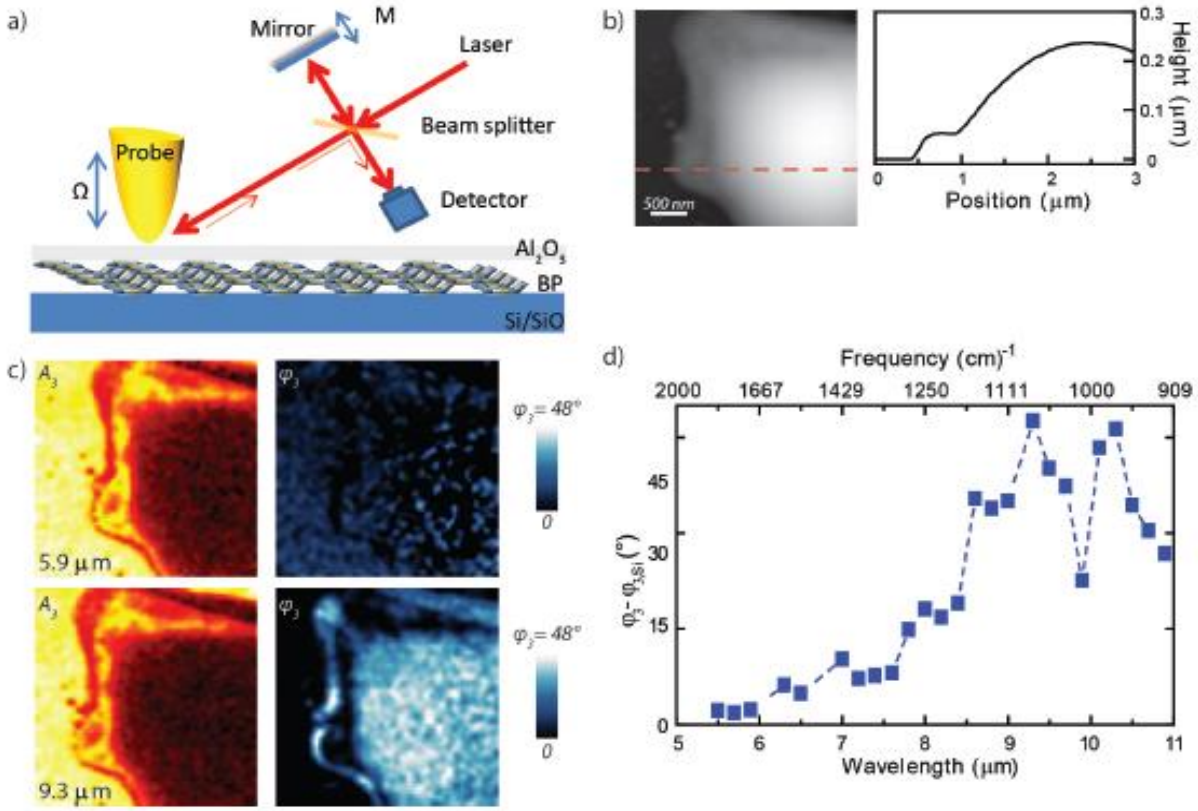

Figure 4.4 (a) Schematic of the s-SNOM experimental setup vertically polarized laser focused on the tip-sample junction produces a near-field interaction with the sample surface, allowing mapping of the local dielectric values of BP surface. (b) Topography image and line profile plot. (c) Third harmonic optical amplitude (A3) and phase (φ3) images at illumination laser wavelength 5.9 μm and 9.3 μm. (d) Normalized s-SNOM phase (φ3) spectroscopy plot of degraded BP.

between the islands, which nearly vanishes at 5.9 μm. In s-SNOM the phase spectral contrast

indicates an absorption in the sample that could be caused by a vibrational mode. To map the absorption spectral response of the sample, we performed phase spectroscopic imaging in the laser wavelength range, λ=5.5 -10.8 μm. For each data point, the same area on the sample was imaged at the specific wavelength and the phase change observed relative to the substrate was plotted. Figure 4.4d shows the experimental near-field optical phase spectrum taken at the degraded parts

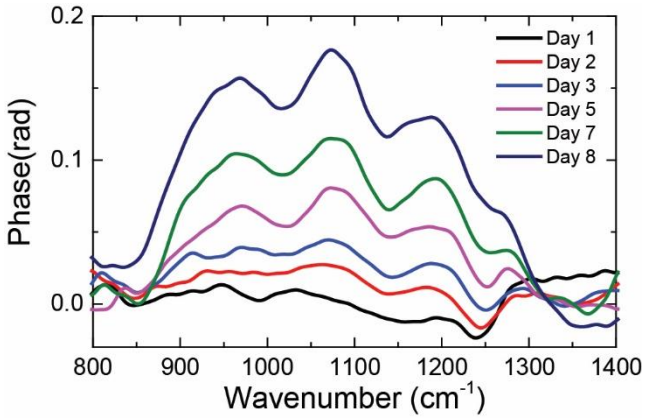

Figure 4.5 Evolution of nano-FTIR spectra of uncoated BP

of the sample normalized by the background phase on the Si substrate. We find a broad near-field phase resonant spectrum that starts around ~7.5 μm. The near-field phase resonance is similar to the far-field absorption peak. This broad infrared band is best assigned to phosphate species that resulted due to ambient degradation following the assignment made in Ref[43] Spectral evolution of uncoated BP has also studied further using nano-FTIR over eight days for the initial stage of degradation process and results are presented in Figure 4.5. The nano-FTIR study was focused on the spectral range 800-1400 cm^{-1} where a broad IR band was observed in the spectrum shown in Figure 4.4d. Figure 4.5 clearly shows that three peaks are gradually evolving as the degradation takes place during eight days, and the peak positions are in good agreement with those seen in the spectrum obtained from nano imaging (Figure 4.4d). Using high-resolution s-SNOM, we further investigated the time evolution of degradation of an unencapsulated exfoliated 27 nm thick BP flake in an ambient environment over the course of more than 90 days. Figure 4.6 displays the

topography (*Figure 4.6*a-k) and near-field optical images (Figure 4.6l-v) taken at a laser wavelength of λ=10.5 μm imaged over a time span of 90 days since exfoliation. In the topographic images, the degraded regions are easily distinguishable from the undegraded regions by higher topography (Figure 4.6 a-k) and lower (darker) contrast in the near-field images (Figure 4.6l-v). The degradation begins soon after exfoliation as nano-sized particles that appear randomly on the surface (Figure 4.6a). The density of these degraded BP nanoparticles (number of degraded BP nanoparticles/unit area) is high in the first few days (1-5 days), however at the intermediate stage (~5-15 days) the nanoparticles density decreases as some of the particles start to become rapidly larger by coalescing with the neighboring degraded regions and eventually degradation covering all of the surface (Figure 4.6k,v). We plotted the measured fraction of the degraded area as a

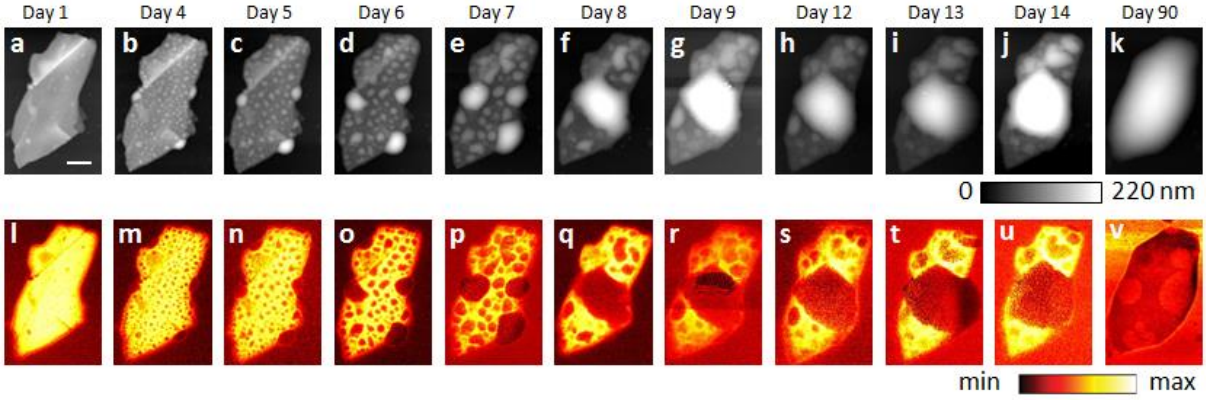

Figure 4.6 Time evolution of topography (a-k) and near-field third harmonic optical amplitude (l-v) taken at laser wavelength of λ=10.5 μm of freshly exfoliated unencapsulated BP with thickness ~27 nm. Scale bar = 500 nm.

function of time in Figure 4.7 . Each data point on the plot (dark squares) represent the sum of the measured area of each degraded bubble divided by the total area of the sample. The degraded surface area was measured using the change in height of a given location on the sample by setting a baseline value for the substrate height for each scan. The experimental graph shows that the degraded area percentage increases with time slowly in the beginning and much faster afterwards before saturating. Similar degradation behavior was observed in other flakes with comparable

thicknesses.

To further understand the degradation process, we use a variant of the forest-fire model to fit our experimental data. We divide the sample surface in $N \times N$ square elements, each of which may exist in one the two states: undegraded BP or degraded BP. Let $\eta^{(n)}$ be the degradation

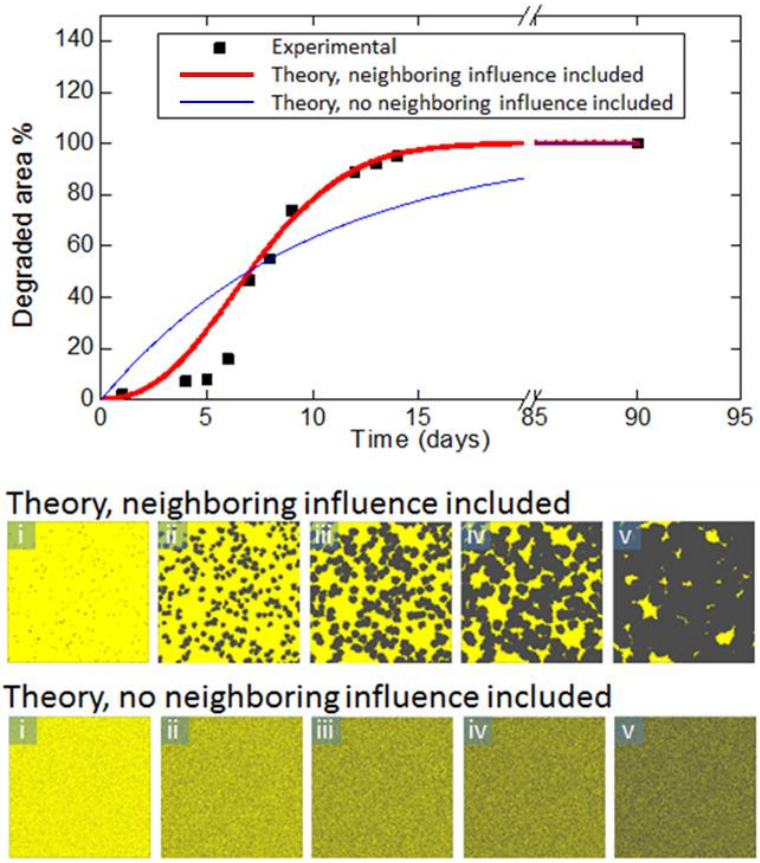

Figure 4.7 Experimental (black squares) and simulated degraded area percentages including neighboring interaction (solid red lines) and with neighboring interactions disregarded (blue red lines). Stages of simulated sample surface during the degradation process (b) corresponds to red curve and (c) corresponds to blue curve.

probability per unit time of a surface element that has n degraded neighbors ($0 \leq n \leq 8$). Consequently, the degradation probability after a small but finite time interval Δt is equal to $P_n = 1 - e^{-\Delta t \cdot \eta^{(n)}}$. For simplicity, we assume that each degraded neighbor increases $\eta^{(n)}$ by a fixed amount $\Delta\eta$, that is, $\eta^{(n)} = \eta^{(0)} + n\Delta\eta$, where $\eta^{(0)}$ is the degradation probability per unit time if

all the immediate neighbors are in the undegraded BP state. We note that our model operates with the degradation probabilities, $\eta^{(n)}$, which can be related to chemical processes that accompany the degradation process such as chemical reaction of BP with O_2 and H_2O to form oxidized phosphorus species. In this way, the model can be used to predict the degradation time evolution under different environmental conditions with varying content of O_2 and H_2O. In the current work, however, we used $\eta^{(n)}$ merely as fitting parameter. We found a good fit to the experimental results, shown in Figure 4.7a, using $\eta^{(0)} = 0$ and $\Delta\eta = 0.45/\text{day}$. For convergence, it was sufficient to use $N = 512$ and $\Delta t = 90$ minutes. We note that if we neglect the influence of neighbors on the degradation probabilities by setting $\Delta\eta = 0$, the model does not predict the experimentally observed results as shown by the blue curve in Figure 4.7a, which is qualitatively different from the measured fraction of degraded surface. Our model strongly suggests that the influence of degraded surface elements on non-degraded ones critically contributes to the degradation process of BP. We also show that $\Delta\eta \neq 0$ leads to the formation of degraded clusters (Figure 4.7b), while neglecting the influence of degraded neighbors results in a homogeneous distribution of degraded surface elements (Figure 4.7c). Thus, taking the influence of degraded neighbors into account qualitatively reproduces experimental images of the surfaces shown in Figure 4.6.

When BP chemically degrades, in addition to the increase of the degraded area, the height of the degraded bubbles also increases vertically on the sample surface. By selecting a single degraded bubble, we have measured the height and volume of the degraded regions as a function of time as shown in *Figure 4.8*. To get each experimental data point (open rectangles) in *Figure 4.8*, the height of the degraded particles was measured from a topographic line profile, and the volume of a bubble was approximated by a spherical cap of height h and base radius a, as shown

in the inset of *Figure 4.8*b. Base radius was measured by drawing three different lines across the center and the average value is used in the formula $V = \frac{\pi h}{6}(3a^2 + h^2)$ of the spherical cap. We

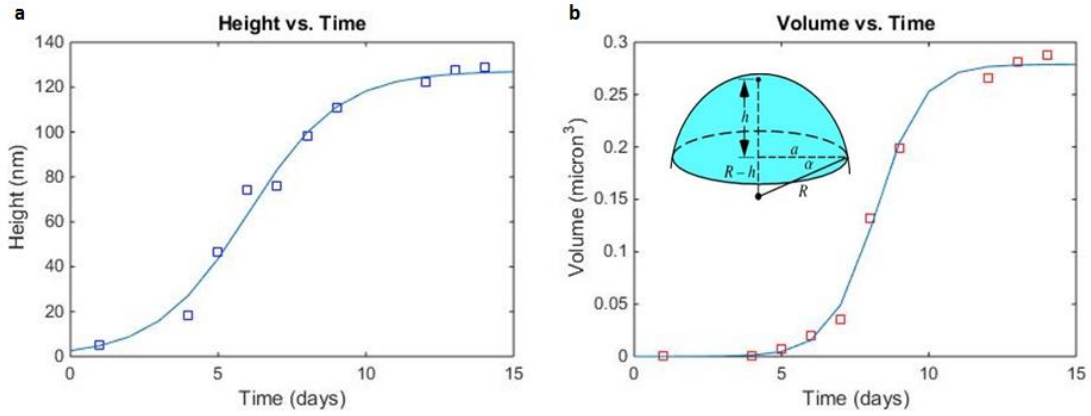

Figure 4.8 Experimental (squares) and simulated (solid lines) of results of height (a) and volume (b) of a degraded bubble. Volume is calculated according to the geometry shown in the inset of (b).

found that both the height (*Figure 4.8*a) and the volume (*Figure 4.8*b) of the degraded regions increase slowly initially and grow in an exponential fashion before reaching saturation growth. Since the modified forest-fire model introduced above is only appropriate for a surface area analysis, we cannot apply it to the experimental height and volume data. However, we used the well-known sigmoid (S-shaped) growth curve to fit the experimental results, as shown by the solid lines in *Figure 4.8*. There is excellent agreement between the experimental and the S-shaped growth curves. Although the S-shaped growth curve, in our case, does not provide any direct physical insight, such as, the contribution of neighborhood interactions introduced above using the modified forest-fire model, the curve fit provides the growth saturation value, the steepness of the growth and the mid-point of the growth, via the three fit parameters typical to S-curves: k, r, and t_0, respectively. From the height fit (the solid line in *Figure 4.8*), we obtained a saturation height of *k =127.21 nm*, a maximum growth steepness of $r = \ddot{0}.65$ day^{-1}, and a mid-point of the growth

of $t_0 = 6.01$ days, which is the time it takes to grow the height to 50% of its saturation value. For the volume curve, we obtained a saturation volume of 0.28 µm3, and the steepness of the volume growth was 1.27 day^{-1}, reaching the 50% of its saturation value within 8.21 days. Although the exact mechanism of the (height/volume) enlargement is beyond the scope of this paper, these fit parameters and the S-curve fit in general may shed light on the three-dimensional growth evolution.

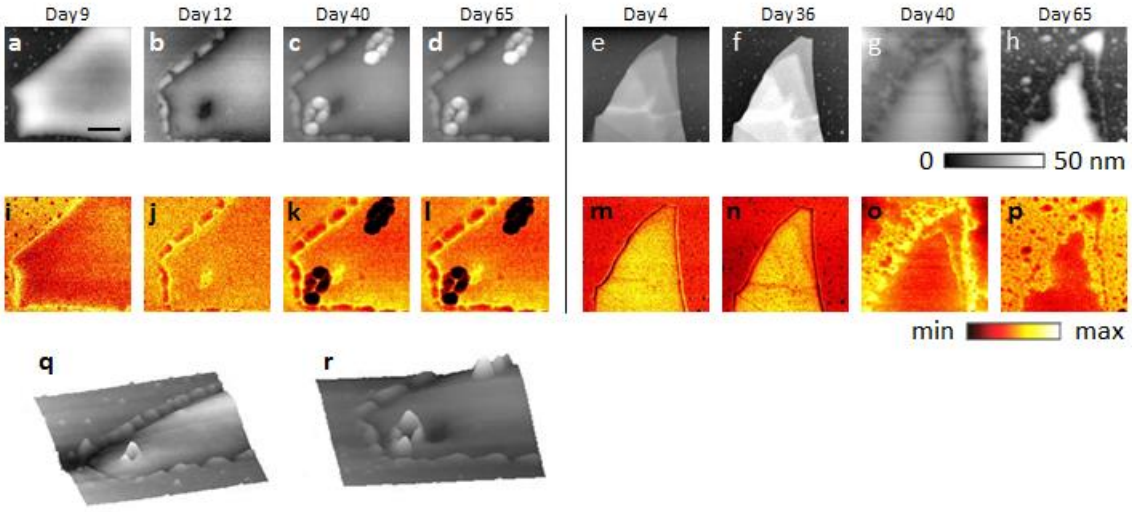

Figure 4.9 Topography (a-h) and third harmonic near-field amplitude (i-p) images of two different flakes of thickness ~5 nm, coated with a 1 nm coating layer of Al_2O_3, (q) and (r) show 3D topographic images of (b) and (c) respectively.

It has been shown that coating BP with Al_2O_3 can passivate from ambient degradation[43]. However, the dependence of the coating effectiveness on its thickness was not studied. Here, we investigate several BP flakes coated with 1 nm, 5 nm, 10 nm, 20 nm and 50 nm thick Al_2O_3 in order to study the effectiveness of the coating in protecting ambient degradation as a function of size over a long period of time. Figure 4.9 shows the evolution of topography and optical near-field images of the two 5 nm thick flakes coated with 1 nm thick Al_2O_3 layer over a span of 65 days. We found that the despite the 1nm protective layer, the underlying BP flake degrades in both cases but at a much reduced rate compared to uncoated samples presented in Figure 4.6. In *Figure*

*4.8*a-h, the degradation starts at the edges of the flake, as well as holes that randomly begin on the surface of the coated layer as clearly seen on the 3D topographic images shown in Figure 4.9q-r. In Figure 4.9e-h, and Figure 4.9m-p we show another 10 nm high BP flake that also coated with 1 nm thick Al_2O_3. In this flake, degradation starts from the edges of the flake and grows inward. We have observed similar degradation of several 1nm Al_2O_3 coated BP flakes with varying thicknesses.

We have also studied the effectiveness of a 5-nm thick Al_2O_3 coating (Figure 4.10) on a 10 nm thick BP flake. We found, similarly to our observations in Figure 4.9 that the BP sample continues to degrade at a yet slower rate than that in the case of a 1-nm coating. The BP flake studied shown in Figure 4.10, initially had randomly scattered nanometer-size degraded bubbles (which possibly arose during/between exfoliation and coating). These initial degraded regions

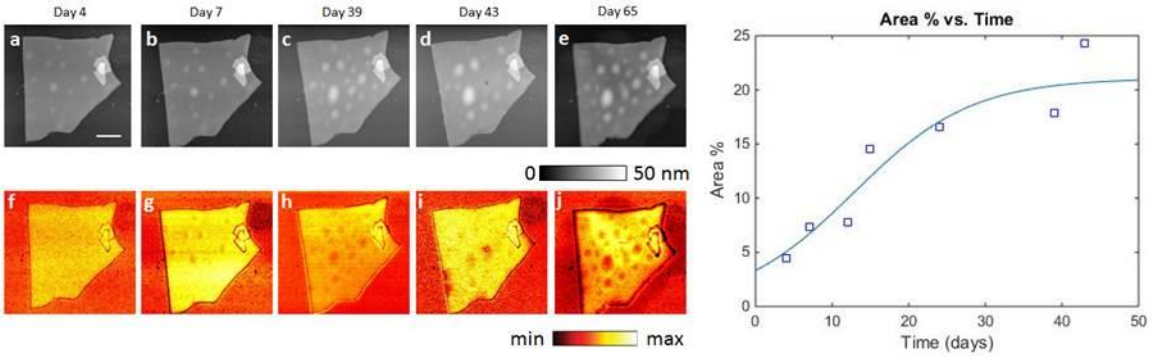

Figure 4.10 Topography (a-e) and third harmonic near-field amplitude (f-j) images of 10 nm BP flake coated with ~5 nm thick Al_2O_3. Experimental (open squares) and simulated (solid blue line) of results of area fraction of the degraded surface.

continue to grow at a slow rate and increase in size, as shown in Figure 4.10e&j. In Figure 4.10 k, the rectangular points present the measured evolution of the degraded area fraction, while the solid line is the theoretical fit. The degraded area was measured following the same procedure as we used to obtain the area shown in Figure 4.7. In comparison to Figure 4.6 (uncoated sample) and Figure 4.9 (1 nm Al_2O_3 coated sample), it can be clearly seen that the degradation takes place at a

slower rate due to the larger thickness (5 nm) of the Al_2O_3 coating. However, since the degradation still increases with time, it is evident that even 5 nm coating of sapphire is insufficient to be considered an ideal passivation of BP underneath it.

We further investigated the effectiveness of thicker Al_2O_3 coatings (thickness 10 nm or more) on various thickness BP flakes by following the degradation behavior over a long period of time. Figure 4.11**a-j** show the topography and near-field optical images of the evolution of 10 nm

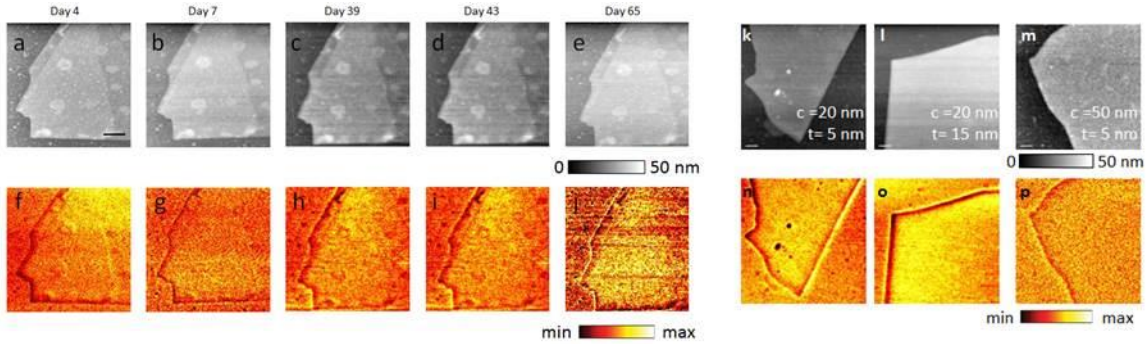

Figure 4.11 Topography (a-e) and A2 (f-j) images of a 5 nm thick BP flake coated with a sapphire layer of 10 nm. Topography (k-m) and near-field amplitude images (n-p) on day 65 of three flakes of different thicknesses, "t" and different sapphire coating layer, "c"; the values of t and c are given in each image from k to m.

Al_2O_3 coated 5 nm thick BP flake. We have also studied 20 nm and, 50 nm thick Al_2O_3 coating as shown in Figure 4.11 k-p. We found no trace of degradation over a long period of time (> 3 months) in all of these samples, which indicates that thicker (10 nm or larger) coating is necessary when using coating of BP by Al_2O_3 using ALD for enhanced passivation of BP over an extended period of time.

4.1.2 Reliable Surface Passivation by Thin Hybrid Coating of BN and Al_2O_3

As per the study reported in Section 4.1.1, finding the experimental approaches to reduce the degradation rate with thin coatings is still a challenge. In this work, we show that a hybrid BN layer (< 2 nm) deposited using metal-organic chemical vapor deposition (MOCVD) technique

followed by 3 nm Al_2O_3 grown using ALD can completely protect BP from degradation for over 45 days.

4.1.2.1 Experimental Details

BP flakes were transferred onto pre-cleaned Si and SiO_2 substrates using conventional mechanical exfoliation. Thin layer of BN and/or Al_2O_3 were then deposited using MOCVD and ALD techniques respectively. Three BP samples were prepared with different coatings and substrates: (i) BP flakes on Si wafer covered by 1.6 nm thin BN layer, (ii) BP flakes on SiO_2 substrate coated with 1.6 nm BN layer, and (iii) BP flakes on SiO2 substrate coated with 1.6 nm thick BN followed by 4 nm thick Al_2O_3. All samples were kept in ambient condition at 22°C with relative humidity ~40%. Topographic and near-field infrared images were taken using s-SNOM. Topography and infrared near-field images of BP flakes allow investigation of the degradation evolution and effectiveness of coatings. For revealing the electrical properties of these encapsulated BP layers, a p-channel metal-oxide field-effect transistor (p-MOSFET) structure was fabricated using 8 nm BP flake with 200 nm channel length (L) and with BN/Al_2O_3 as gate dielectric. Details of the p-MOSFET device fabrication and electrical measurement procedures can be found in ref. [23]

4.1.2.2 Results and Discussion

Figure 4.12 shows topography and third harmonic near-field amplitude (A_3) images of eight BP flakes. Those are with thicknesses ~30 nm (Figure 4.12a, b and c), ~8 nm (Figure 4.12d, e and f), ~5 nm (Figure 4.12g) and ~15 nm (Figure 4.12h). All exfoliated samples were passivated with either BN (Figure 4.12a, b, d and e), hybrid BN-Al_2O_3 (Figure 4.12c and f) or Al2O3 (Figure

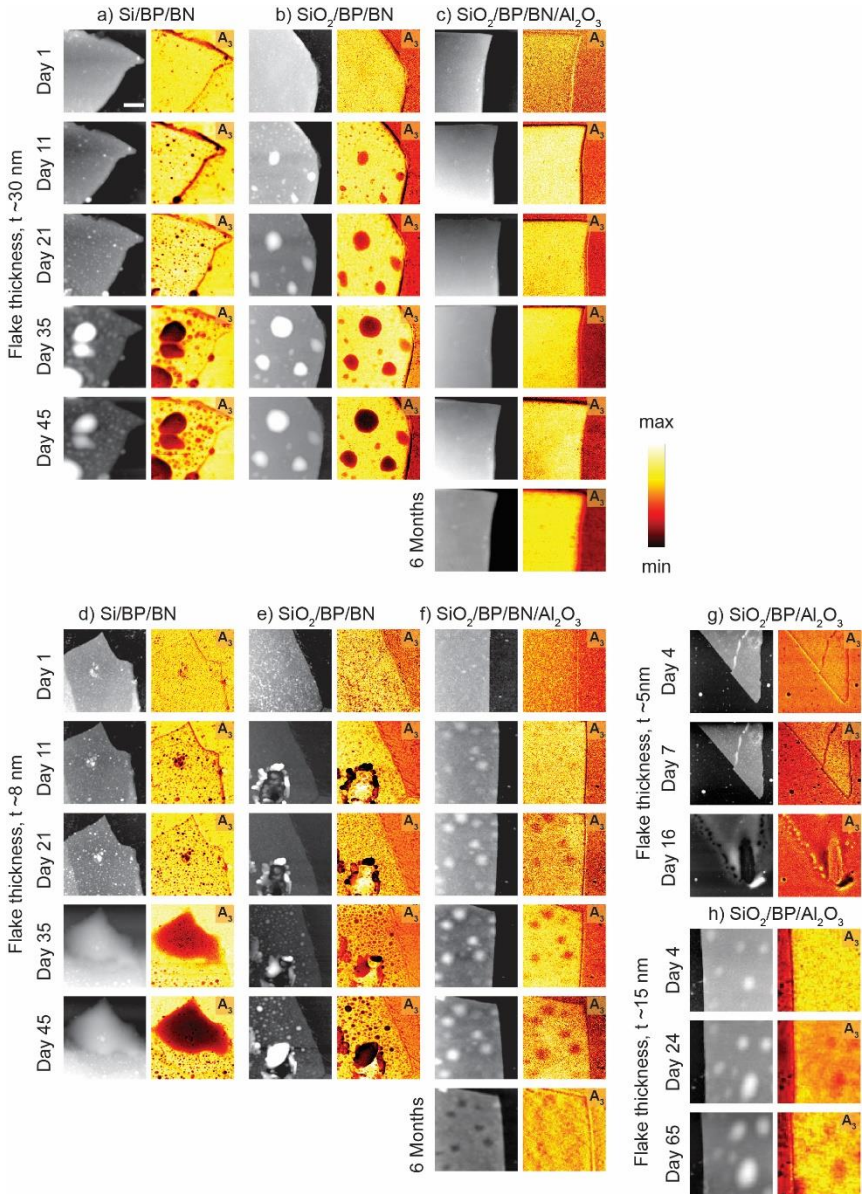

Figure 4.12 The topography (grey-white) and 3rd harmonic near-field amplitude, A3 (red-yellow) images of BP on Si (a and d) and SiO_2 (b, c, e, f, g and h) substrates. The flakes are encapsulated by BN (a, b, d and e), hybrid coating of BN-Al_2O_3 (c and f), and by Al_2O_3 (g and h) layers. Scale bar 500 nm.

4.12g and h) coatings. We took successive images of all samples shown in Figure 4.12 for over 45 days but only displayed certain selected images with day # from each flake for comparison.

As shown in Figure 4.12-a, b, d & e 1.6 nm BN coating is robust and protects degradation in both the 8 nm and 30 nm thick flakes until about day 11 after exfoliation. After the 11th day, the 8 nm thick flake raptures the BN coating and begins to degrade forming bubbles that grow in size as a function of time. Whereas the 30 nm thick BP flake begins with small bubbles that enlarge with time after the 11th day. The rate of degradation is much slower in the 30 nm thick BP flake compared to the 8 nm flake of the same coating. BN coating keeps the BP flakes intact regardless of thickness for 11 days and the degradation afterwards proceeds at much slower rate compared to uncoated BP. We have shown two Al_2O_3 coated BP flakes of thickness 5 nm (Figure 4.12g) and 15 nm (Figure 4.12h). The Al_2O_3 coating layer for these two are 1 nm and 5 nm, respectively. The 5 nm flake coated with 1 nm Al_2O_3 degraded rapidly and ruptured by day 16. However, the 5 nm Al_2O_3 coating of 15 nm thick flake has decelerated the degradation process significantly, but sporadically evolved bubbles were prominent by day 65. A detailed account on the effect of Al_2O_3 coating of BP has been given in Section 4.1.1. Other studies of BN-BP-BN sandwiched stable heterostructures have been reported before, however the degradation of BP was not monitored beyond a week to assess the effectiveness of the coating.[10]

Hybrid BN (1.6 nm thick) plus Al_2O_3 (4 nm thick) coated BP flakes of thickness 8 nm and 30 nm are shown in in Figure 4.12-c & f. Over the time span of our measurement (~45 days) the 30 nm BP flake did not show any sign of degradation. The thinner 8 nm double coated flake showed slightly degraded by day 11 and increased very slowly till day 45 as shown in Figure 4.12f. Our results unequivocally show that hybrid BN (MOCVD) and Al_2O_3 (ALD) coating completely

avoids degradation of BP flakes for thickness ~30 nm and significantly slows down degradation for thinner (~8 nm thick) BP flakes over a period of a month and half.

We have also investigated the effect of the substrate on which BP flakes are exfoliated on the degradation. Figure 4.13 shows the topography and near-field amplitude of two BP flakes (thickness 8 nm and 30 nm) exfoliated on Si and SiO_2 substrates and both covered by 1.6 nm BN.

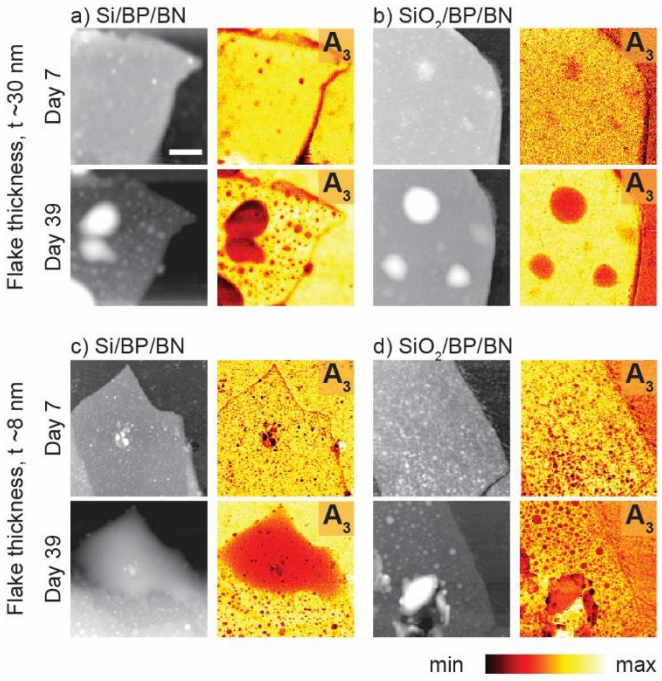

Figure 4.13 The topography (grey-white) and 3rd harmonic near-field amplitude (red-yellow) images of the flakes of Si/BP/BN with thickness ~30 nm (a) and ~8 nm (c) and flakes of SiO_2/BP/BN with thickness ~30 nm (b) and ~8 nm (d) on day 7 and day 39. Scale bar 500 nm.

These images show that both the 8 nm and 30 nm thick flakes exfoliated on Si wafer show larger degraded area in a similar duration to those exfoliated on SiO_2. When the height of the tallest degradation 'bubble' on the thicker flakes of these two samples are compared, it shows that the bubble height of the flake on SiO_2 is ~50% smaller than that of the flake on the Si substrate. Both the area coverage and the volume of the degraded bubbles suggest that BP exfoliated on SiO_2 substrate degrades at a slower rate. These results further suggest that it is important to select not

only coating material but also the substrate on which to exfoliate/grow BP to reduce degradation.[10] We also note the near-field contrast of BP on Si substrate is larger than that on SiO2 due to the larger permittivity of Si ($\varepsilon_{Si} > \varepsilon_{BP} > \varepsilon_{SiO2}$).

We implemented the model explained in Section 4.1.1 to understand the evolution of the degradation process of the samples investigated experimentally. In this model, the sample surface is divided in to *N* x *N* square elements that were randomly defined to be in degraded or non-degraded state. For each of these elements the number of degraded neighbor elements, $n\ (0 < n < 8)$ were correlated to the degradation probability of the considered element. We considered two cases *(i)* inclusion, and *(ii)* exclusion of the influence of neighboring elements on the degradation of a given element. Experimental data in our previous study were well fitted with the model that considers case *(i)* where inclusion of the influence of neighbors was a considerable factor.[46a] In this experiment we found that as the passivation becomes more robust such as using hybrid coating, the evolution of percent degradation as a function of time does not depend on the influence of neighbors as described further below.

In Figure 4.14, we show in blue circles the degradation area percentage as a function of time extracted from the experiments for each of the six flakes described in Figure 4.12 and discussion thereof. The red lines in Figure 4.14 show the fitting result of percent degradation of each flake, based on our mathematical model[46a]. Of all the samples studied, both 8 nm and 30 nm thick BP flakes exfoliated on Si wafer and coated only with BN layer are the samples with highest rate of degradation. As shown in Figure 4.14a & d, for these samples the model that considers

inclusion of influence of the neighboring elements on the degradation (case *i*) agrees well with the experimental data. However, for the flakes with slower degradation, fitting significantly failed to

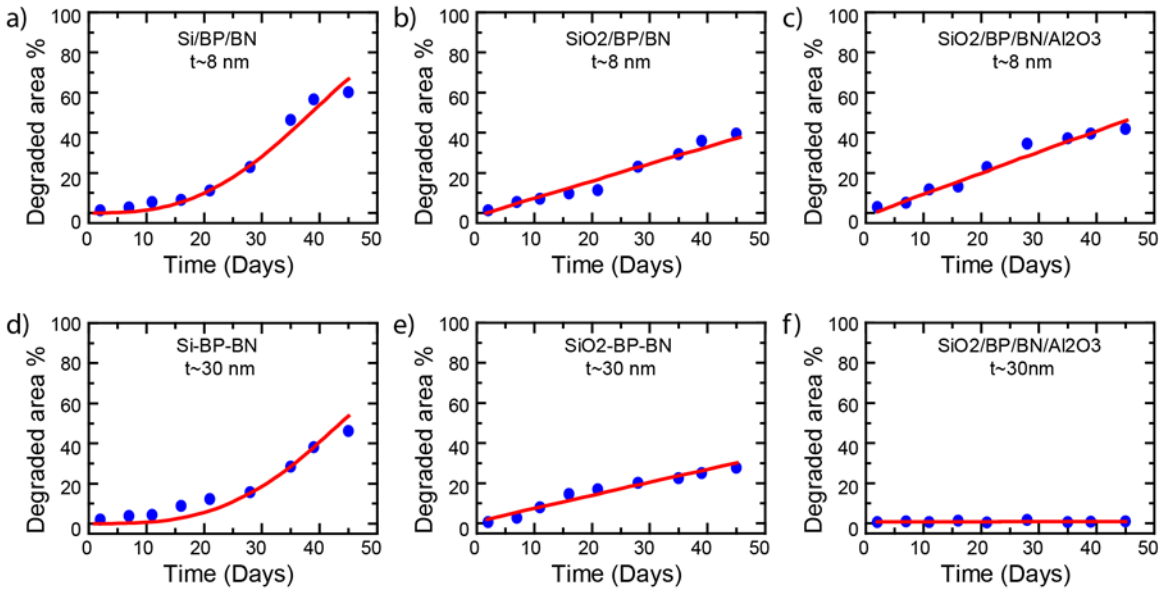

Figure 4.14 Evolution of degradation area percentage of six flakes shown in fig. 1 over the duration of 45 days plotted (blue dots) together with the fitting (red lines) results.

represent the experimental results when neighbor influence is considered in calculations. Surprisingly, when the neighbor influence is excluded in calculations the model fitted the experimental data in a very good agreement as shown in Figure 4.14b, c & e resulting in an almost-linear relationship between degradation area percentage and time. This behavior suggests that the neighbor influence on degradation of a given site is significantly suppressed in the SiO_2/BP/BN and SiO_2/BP/BN/Al_2O_3 samples. Moreover, according to the topography and near-field amplitude images shown in Figure 4.12f, and degradation % vs. time in Figure 4.14f, the 30 nm flake on SiO_2 coated with BN and Al_2O_3 shows significant protection from degradation. We also note thickness dependent degradation of BP has been explained recently by the decrease in bandgap with increasing layer thickness that leads to a decrease in oxygen acceptance rate.[50]

The output characteristics of the drain current (I_d) vs. drain voltage (V_{ds}) of a BN/Al_2O_3 top-gate BP MOSFET the device are shown in Fig. 4a. The highest drain current, Id = 800 μA/μm was achieved at Vd = -1.6 V and gate voltage, Vg =-4 V. The low contact resistance and high hole

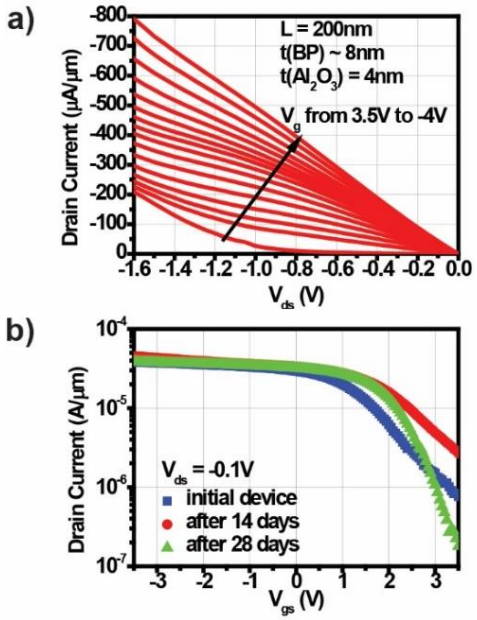

Figure 4.15 (a) Output characteristics of a BP MOSFET with BN/Al_2O_3 as bi-layer gate dielectric. The high electron transport from the drain contact at high V_{ds} leading to degradation of off-state of the device. (b)Time dependence of drain current, Id vs. V_{gs} of a BP MOSFET with Ni/Au as contact metals. The device has minor off-state changes after four week.

mobility of BP lead to the high on-state drain current of this device. However, due to the narrow bandgap of BP, the electron Schottky barrier is low in general, in great contrast to transition metal dichalcogenides such as MoS_2, ambipolar effect degrades the off-state of the device, which leads to a significant current at large drain voltage. In order to study how the device performance changes with time, the I_d-V_{gs} transfer characteristics measurements were performed after fabrication, and after 14 days and 28 days stored in nitrogen box, with V_d = -0.1 V. These time dependent I_d-V_{gs} curves are presented in Figure 4.15b. Even after 28 days, the device still worked with small changes at off-state such as a minor shift in threshold voltage observed on day 14 and day 28

curves. Without BN/Al_2O_3 encapsulation, the device does not survive over 24 hours due to the strong chemical reaction of BP with moisture in ambient. The electrical characterizations are also consistent with the surface analysis described above.

4.1.3 Summary and Conclusion

In summary, we have extensively investigated ambient degradation of exfoliated BP with and without a thin Al_2O_3 coating layer using the unique simultaneous topographic and nano-scale spectroscopic imaging capabilities of s-SNOM. By measuring several BP flakes coated with varying thickness Al_2O_3 deposited by atomic layer deposition (ALD) over a span of several months, we show that the degraded area and volume increase with time slowly in the beginning of degradation and grow rapidly (approximately exponentially) afterwards before reaching saturation growth following S-shaped growth curve (sigmoid growth curve).Our mathematical modeling of the experimental degradation growth pattern shows that the influence of degraded areas on their adjacent environment is the cause of the observed exponential growth at the initial stage of degradation growth pattern. We found that the thickness and quality of coating is critical to effectively passivate BP from ambient degradation. Oxidized phosphorus species, chemical identified using nanoscale spectroscopic imaging by s-SNOM, can still form underneath 5 nm or less thick Al_2O_3 coating which renders thin coatings insufficient to protect BP against degradation.

Based on both surface analysis and electrical measurements, we have shown that the surface stability of BP can be significantly improved by a hybrid ~5nm coating of BN/Al_2O_3. Even after 45 days, no sign of surface degradation was observed on ~30 nm BP flake. The electrical properties of pMOSFET device structure with BN/Al_2O_3 as gate produced excellent drain current of 800 μA/μm promising the use of this technique for further development of BP based electrical devices.

4.2 Nanoscopy of Muscovit Mica

4.2.1 Introduction

Muscovite type mica is an inorganic material with very interesting physical properties. It is most commonly used as an insulator, but mica also contains many characteristics needed for organic field-effect transistors (OFET).[51] Micas atomically flat surface and supreme stability will provide a boost in high performance electronics.[51a, 52] With a dielectric constant of 6.4-9.3, mica stands out as one of the most promising materials to use as gate dielectrics.[51b, 53] Extensive studies of the nanoscopic physical properties of mica have not much been reported in literature. In this section we present some of the nanoimaging and nanospectroscopic results we obtained for exfoliated mica samples on Si and SiO_2 substrates.

4.2.2 Experimental Details and Results

Flakes of mica were mechanically exfoliated onto a Si or SiO_2 wafers.. The samples were placed on a stage where a p-polarized quantum cascade laser is focused on the tip and sample for nano imaging. Using pseudoheterodyne detection, the scattered beam was collected and sent to the linear polarizer along with the reference beam. The linear polarizer filters out all signal other than the p-polarized signal, which is used for analysis. In order to study the influence of the substrate on the spectrum of mica on both Si and SiO_2, a SiO_2 sample on Si has also been analyzed using nano-FTIR.

Figure 4.16 shows the near-field 2nd harmonic amplitude and phase images of SiO_2 thin film on Si taken at 1000 cm^{-1} (a, b), 1175 cm^{-1} (c, d) and 1325 cm^{-1} (e, f). Figure 4.16g shows the spectra obtained from nanoimaging (black line with dots) nano-FTIR (red line) in the range 900 – 1500 cm^{-1} for a 60 nm thick flake; the inset shows the topography of the flake. The near-field

contrast changes with wavelength. As seen in Figure 4.16b, d and f, phase contrast is very low at 1000cm^{-1} and very high at 1175 cm^{-1}; at 1325 cm^{-1} shows a weaker phase contrast.

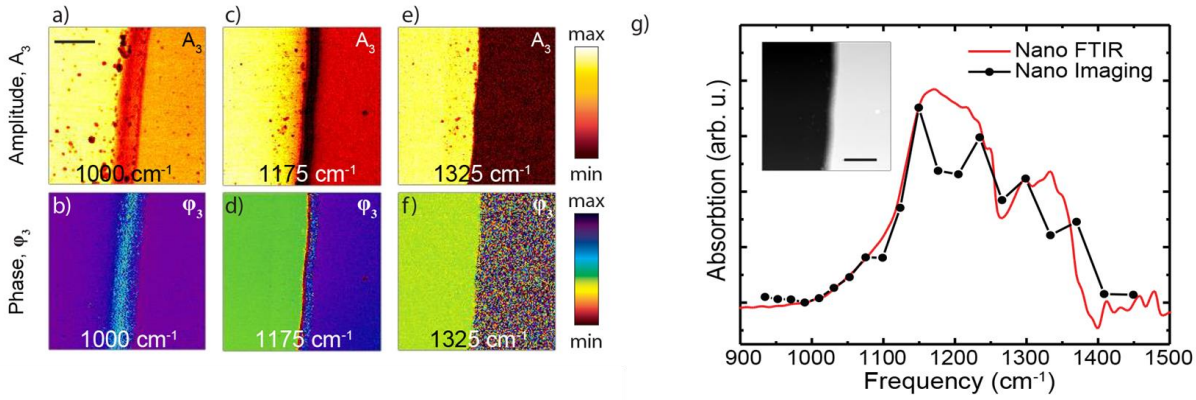

Figure 4.16 Nanoimaging and spectra of SiO_2 on Si. Third harmonic near-field amplitude (a, c and e) and phase (b, d and f) of SiO_2 on Si at three different frequencies. IR spectra obtained from nano-imaging (black line) and nano-FTIR (red line) with topography image of the same area in the inset (g). Scale bar 500 nm.

The near-field 2nd harmonic amplitude and phase images of a mica flake on Si taken at 950 cm^{-1} (a, b), 1050cm^{-1} (c, d) and 1200 cm^{-1} (e, f) are presented in Figure 4.17. Figure 4.16g shows the spectra obtained from nanoimaging (black line with dots) nano-FTIR (red line) in the range

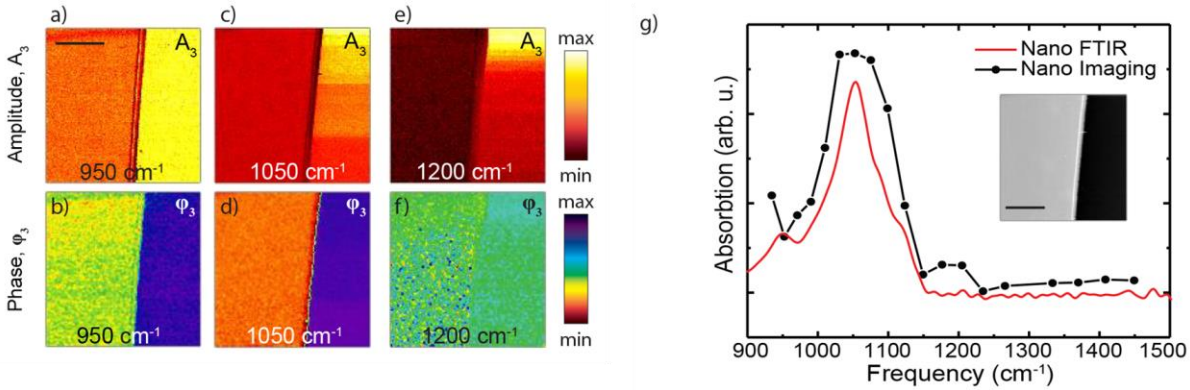

Figure 4.17 Nanoimaging and spectra of mica on Si. Third harmonic near-field amplitude (a, c and e) and phase (b, d and f) of mica on Si at three different frequencies. IR spectra obtained from nano-imaging (black line) and nano-FTIR (red line) with topography image of the same area in the inset (g). Scale bar 500 nm. Scale bar 500 nm.

900– 1500 cm^{-1} for a 65 nm thick flake; the inset shows the topography of the flake. As seen in Figure 4.17b, d and f, phase contrast between mica flake and Si substrate is greatly increasing from

950 cm^{-1} to 1050 cm^{-1} and extremely lower at 1200 cm^{-1}; at 1200 cm^{-1} shows a weaker phase contrast.

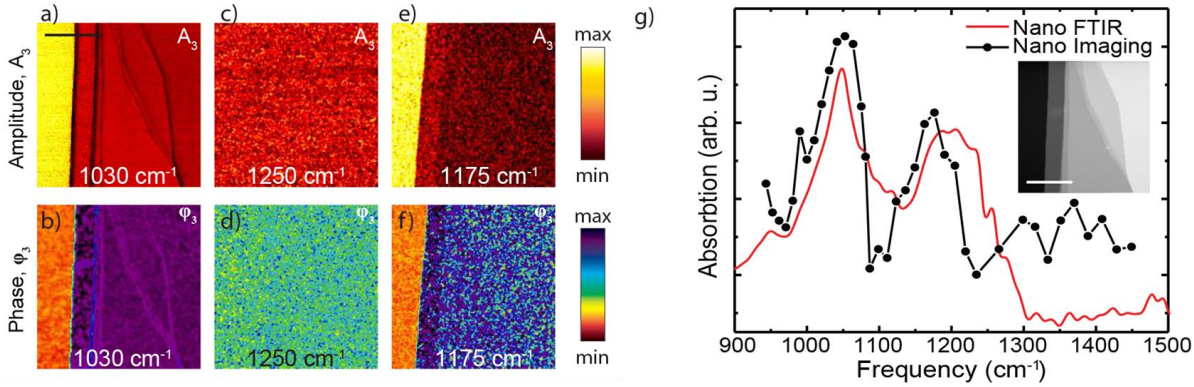

Figure 4.19 Nanoimaging and spectra of mica on SiO_2. Third harmonic near-field amplitude (a, c and e) and phase (b, d and f) of SiO_2 on Si at three different frequencies. IR spectra obtained from nano-imaging (black line) and nano-FTIR (red line) with topography image of the same area in the inset (g). Scale bar 500 nm. Scale bar 500 nm.

Figure 4.18 shows the near-field 2nd harmonic amplitude and phase images of a mica flake on SiO_2 substrate taken at 1030 cm^{-1} (a, b), 1350cm^{-1} (c, d) and 1175 cm^{-1} (e, f). The spectra shown in Figure 4.16g are obtained from nanoimaging (black line with dots) nano-FTIR (red line) in the range 900– 1500 cm^{-1} for a ~135 nm thick flake; the inset shows the topography of the flake. As seen in Figure 4.18b, d and f, the highest phase contrast is observed at 1030 cm^{-1} and almost no

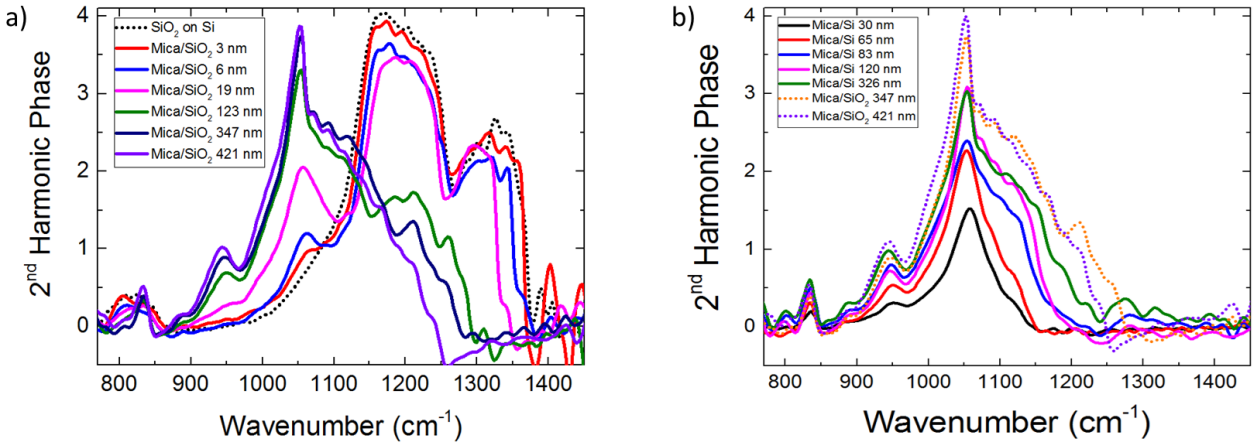

Figure 4.18 Thickness dependent spectra of mica on SiO_2 (a) and on Si (b).

contrast is seen at 1350cm^{-1}. At 1175 cm^{-1} it shows a certain phase contrast but weaker than that at 1030 cm^{-1}.

The thickness dependence of the phase spectra of mica on both Si and SiO_2 are extensively studied using nano-FTIR spectroscopy and presented the results in Figure 4.19. The spectra from six mica flakes (solid lines) on SiO_2 with different thicknesses ranging from 3 nm to 421 nm are compared with a spectrum of a SiO_2 film (dotted line) in Figure 4.19a; the intensity of the peaks at ~1200 cm^{-1} and 1340 cm^{-1} in mica spectra are getting weaker with increasing mica flake thickness. These two peaks are very pronounced in the flakes with lower thickness (<20 nm).

Figure 4.19b shows the five spectra of mica flakes (solid lines) with different thicknesses in the range of 30 nm to 326 nm compared with two spectra of mica on SiO_2 (dotted lines) from flakes with thicknesses 347 and 421 nm. For the flakes with smaller thicknesses (<70 nm), there appears a one strong peak around 1060 cm^{-1}. However, with increasing flake thickness there is a shoulder to this peak emerging from the higher energy side. This evidently overlaps with the broader peak observed in the spectra of thicker mica flakes on SiO_2.

4.2.3 Summary and Conclusion

In summary, we have performed an extensive infrared spectroscopic investigation of exfoliated mica on Si and SiO_2 substrates using the unique simultaneous topographic and nano-scale spectroscopic imaging of nano-FTIR. The wavelength dependent phase contrast is observed for mica on both Si and SiO_2 substrates. This can be explained by the difference in the dielectric properties of mica, Si and SiO_2. A clear thickness dependence of the spectral peaks is observed in mica flakes exfoliated on both substrates. In order for a conclusive understanding of these variations in the peaks, further studies are needed using a suitable computational model.

REFERENCES

1. Abbe, E., Beiträge zur Theorie des Mikroskops und der mikroskopischen Wahrnehmung. *Archiv für mikroskopische Anatomie* **1873,** *9* (1), 413-418.

2. Rayleigh, XXXI. Investigations in optics, with special reference to the spectroscope. *Philosophical Magazine Series 5* **1879,** *8* (49), 261-274.

3. (a) Synge, E. H., XXXVIII. A suggested method for extending microscopic resolution into the ultra-microscopic region. *The London, Edinburgh, and Dublin Philosophical Magazine and Journal of Science* **1928,** *6* (35), 356-362; (b) Synge, E. H., III. A microscopic method. *The London, Edinburgh, and Dublin Philosophical Magazine and Journal of Science* **1931,** *11* (68), 65-80; (c) Synge, E. H., XXIII. An application of piezo-electricity to microscopy. *The London, Edinburgh, and Dublin Philosophical Magazine and Journal of Science* **1932,** *13* (83), 297-300.

4. Ash, E. A.; Nicholls, G., Super-resolution Aperture Scanning Microscope. *Nature* **1972,** *237* (5357), 510-512.

5. Novotny, L.; Hecht, B., Theoretical foundations. In *Principles of Nano-Optics*, Cambridge University Press: Cambridge, 2006.

6. Knoll, B.; Keilmann, F., Electromagnetic fields in the cutoff regime of tapered metallic waveguides. *Optics Communications* **1999,** *162* (4-6), 177-181.

7. Lahrech, A.; Bachelot, R.; Gleyzes, P.; Boccara, A. C., Infrared-reflection-mode near-field microscopy using an apertureless probe with a resolution of λ/600. *Opt. Lett.* **1996,** *21* (17), 1315-1317.

8. (a) Lahrech, A.; Bachelot, R.; Gleyzes, P.; Boccara, A. C., Infrared near-field imaging of implanted semiconductors: Evidence of a pure dielectric contrast. *Applied Physics Letters* **1997,** *71* (5), 575-577; (b) Huber, A. J.; Kazantsev, D.; Keilmann, F.; Wittborn, J.; Hillenbrand, R.,

Simultaneous IR Material Recognition and Conductivity Mapping by Nanoscale Near-Field Microscopy. *Advanced Materials* **2007,** *19* (17), 2209-2212.

9. Knoll, B.; Keilmann, F., Near-field probing of vibrational absorption for chemical microscopy. *Nature* **1999,** *399* (6732), 134-137.

10. Hillenbrand, R.; Taubner, T.; Keilmann, F., Phonon-enhanced light-matter interaction at the nanometre scale. *Nature* **2002,** *418* (6894), 159-162.

11. Knoll, B.; Keilmann, F., Enhanced dielectric contrast in scattering-type scanning near-field optical microscopy. *Optics Communications* **2000,** *182* (4-6), 321-328.

12. Gozhenko, V. V.; Grechko, L. G.; Whites, K. W., Electrodynamics of spatial clusters of spheres: Substrate effects. *Physical Review B* **2003,** *68* (12), 125422.

13. (a) Cvitkovic, A.; Ocelic, N.; Hillenbrand, R., Analytical model for quantitative prediction of material contrasts inscattering-type near-field optical microscopy. *Opt. Express* **2007,** *15* (14), 8550-8565; (b) Stiegler, J. M.; Abate, Y.; Cvitkovic, A.; Romanyuk, Y. E.; Huber, A. J.; Leone, S. R.; Hillenbrand, R., Nanoscale infrared absorption spectroscopy of individual nanoparticles enabled by scattering-type near-field microscopy. *ACS Nano* **2011,** *5* (8), 6494-9.

14. Yohannes Abate, D. S., Alireza Fali, Sampath Gamage, Viktoriia E. Babicheva, Vladislav S. Yakovlev, Mark I. Stockman, Ramon Collazo, Dorian Eduardo Alden, and Nikolaus Dietz, Nanoscopy of Phase Separation in InxGa1-xN Alloys. *ACS Appl. Mater. Interfaces* **2016,** *DOI: 10.1021/acsami.6b06766.*

15. (a) Wickramasinghe, H. K.; Williams, C. C., Apertureless near field optical microscope. Google Patents: 1990; (b) Keilmann, F.; Hillenbrand, R., Near-field microscopy by elastic light scattering from a tip. *Philosophical Transactions of the Royal Society of London. Series A: Mathematical, Physical and Engineering Sciences* **2004,** *362* (1817), 787-

805; (c) Stiegler, J. M.; Abate, Y.; Cvitkovic, A.; Romanyuk, Y. E.; Huber, A. J.; Leone, S. R.; Hillenbrand, R., Nanoscale Infrared Absorption Spectroscopy of Individual Nanoparticles Enabled by Scattering-Type Near-Field Microscopy. *ACS Nano* **2011,** *5* (8), 6494-6499; (d) Abate, Y., Near-Field Spectroscopy and Imaging of Single Nanoparticles. In *Dekker Encyclopedia of Nanoscience and Nanotechnology, Third Edition*, CRC Press: 2014; pp 1-11.

16. (a) Wurtz, G.; Bachelot, R.; Royer, P., A reflection-mode apertureless scanning near-field optical microscope developed from a commercial scanning probe microscope. *Review of Scientific Instruments* **1998,** *69* (4), 1735-1743; (b) Hillenbrand, R.; Keilmann, F., Complex optical constants on a subwavelength scale. *Physical Review Letters* **2000,** *85* (14), 3029-3032; (c) Labardi, M.; Patane, S.; Allegrini, M., Artifact-free near-field optical imaging by apertureless microscopy. *Appl. Phys. Lett.* **2000,** *77*, 621.

17. (a) Yasuo, S.; Hiroko, S., Heterodyne Detection for the Extraction of the Probe-Scattering Signal in Scattering-Type Scanning Near-Field Optical Microscope. *Japanese Journal of Applied Physics* **2000,** *39* (4A), L321; (b) Roy, D.; Leong, S. H.; Welland, M. E., Dielectric Contrast Imaging Using Apertureless Scanning Near-Field Optical Microscopy in the Reflection Mode. *Journal of the Korean Physical Society* **2005,** *47* (Aug. 2005), 7.

18. Ocelic, N.; Huber, A.; Hillenbrand, R., Pseudoheterodyne detection for background-free near-field spectroscopy. *Applied Physics Letters* **2006,** *89* (10), 101124.

19. Vaez- Iravani, M.; Toledo- Crow, R., Phase contrast and amplitude pseudoheterodyne interference near field scanning optical microscopy. *Applied Physics Letters* **1993,** *62* (10), 1044-1046.

20. Harris, A.; Cardone, G.; Winkler, D. C.; Heymann, J. B.; Brecher, M.; White, J. M.; Steven, A. C., Influenza virus pleiomorphy characterized by cryoelectron tomography. *Proceedings of the National Academy of Sciences* **2006,** *103* (50), 19123-19127.

21. (a) Greber, U. F., Virus and Host Mechanics Support Membrane Penetration and Cell Entry. *Journal of Virology* **2016,** *90* (8), 3802-3805; (b) Fontana, J.; Steven, A. C., Influenza virus-mediated membrane fusion: Structural insights from electron microscopy. *Archives of Biochemistry and Biophysics* **2015,** *581*, 86-97.

22. (a) Amenabar, I.; Poly, S.; Nuansing, W.; Hubrich, E. H.; Govyadinov, A. A.; Huth, F.; Krutokhvostov, R.; Zhang, L.; Knez, M.; Heberle, J.; Bittner, A. M.; Hillenbrand, R., Structural analysis and mapping of individual protein complexes by infrared nanospectroscopy. *Nature Communications* **2013,** *4*, 2890; (b) Khatib, O.; Wood, J. D.; McLeod, A. S.; Goldflam, M. D.; Wagner, M.; Damhorst, G. L.; Koepke, J. C.; Doidge, G. P.; Rangarajan, A.; Bashir, R.; Pop, E.; Lyding, J. W.; Thiemens, M. H.; Keilmann, F.; Basov, D. N., Graphene-Based Platform for Infrared Near-Field Nanospectroscopy of Water and Biological Materials in an Aqueous Environment. *ACS Nano* **2015,** *9* (8), 7968-7975; (c) Bechtel, H. A.; Muller, E. A.; Olmon, R. L.; Martin, M. C.; Raschke, M. B., Ultrabroadband infrared nanospectroscopic imaging. *Proceedings of the National Academy of Sciences* **2014,** *111* (20), 7191-7196.

23. (a) Huth, F.; Govyadinov, A.; Amarie, S.; Nuansing, W.; Keilmann, F.; Hillenbrand, R., Nano-FTIR Absorption Spectroscopy of Molecular Fingerprints at 20 nm Spatial Resolution. *Nano Letters* **2012,** *12* (8), 3973-3978; (b) Atkin, J. M.; Berweger, S.; Jones, A. C.; Raschke, M. B., Nano-optical imaging and spectroscopy of order, phases, and domains in complex solids. *Advances in Physics* **2012,** *61* (6), 745-842; (c) Grefe, S. E.; Leiva, D.; Mastel, S.; Dhuey, S. D.; Cabrini, S.; Schuck, P. J.; Abate, Y., Near-field spatial mapping of strongly interacting multiple

plasmonic infrared antennas. *Physical Chemistry Chemical Physics* **2013,** *15* (43), 18944-18950; (d) Nuno, Z.; Hessler, B.; Ochoa, J.; Shon, Y. S.; Bonney, C.; Abate, Y., Nanoscale subsurface- and material-specific identification of single nanoparticles. *Optics Express* **2011,** *19* (21), 20865-20875; (e) Taubner, T.; Hillenbrand, R.; Keilmann, F., Performance of visible and mid-infrared scattering-type near-field optical microscopes. *Journal of Microscopy-Oxford* **2003,** *210*, 311-314; (f) Cvitkovic, A.; Ocelic, N.; Aizpurua, J.; Guckenberger, R.; Hillenbrand, R., Infrared imaging of single nanoparticles via strong field enhancement in a scanning nanogap. *Physical Review Letters* **2006,** *97* (6), -; (g) Huber, A.; Ocelic, N.; Kazantsev, D.; Hillenbrand, R., Near-field imaging of mid-infrared surface phonon polariton propagation. *Applied Physics Letters* **2005,** *87* (8), 081103-1-3.

24. Surewicz, W.; Mantsch, H., Infrared Absorption Methods for Examining Protein Structure. In *Spectroscopic methods for determining protein structure in solution*, Havel, H. A., Ed. Berlin, 1996; pp xii, 250 p.

25. (a) Fontana, J.; Cardone, G.; Heymann, J. B.; Winkler, D. C.; Steven, A. C., Structural Changes in Influenza Virus at Low pH Characterized by Cryo-Electron Tomography. *Journal of Virology* **2012,** *86* (6), 2919-2929; (b) Lee, K. K., Architecture of a nascent viral fusion pore. *The EMBO Journal* **2010,** *29* (7), 1299-1311.

26. Hastings, G.; Wang, R.; Krug, P.; Katz, D.; Hilliard, J., Infrared microscopy for the study of biological cell monolayers. I. Spectral effects of acetone and formalin fixation. *Biopolymers* **2008,** *89* (11), 921-930.

27. Lewis, R. N.; McElhaney, R. N.; Pohle, W.; Mantsch, H. H., Components of the carbonyl stretching band in the infrared spectra of hydrated 1,2-diacylglycerolipid bilayers: a reevaluation. *Biophysical Journal* **1994,** *67* (6), 2367-2375.

28. Lewis, R. N. A. H.; McElhaney, R. N., Membrane lipid phase transitions and phase organization studied by Fourier transform infrared spectroscopy. *Biochimica et Biophysica Acta (BBA) - Biomembranes* **2013,** *1828* (10), 2347-2358.

29. Hull, M. C.; Cambrea, L. R.; Hovis, J. S., Infrared Spectroscopy of Fluid Lipid Bilayers. *Analytical Chemistry* **2005,** *77* (18), 6096-6099.

30. Mathlouthi, M.; Koenig, J. L., Vibrational Spectra of Carbohydrates. *Advances in Carbohydrate Chemistry and Biochemistry* **1987,** *44*, 7-89.

31. Prathiba, J.; Malathi, R., Probing RNA–antibiotic interactions: a FTIR study. *Molecular Biology Reports* **2008,** *35* (1), 51-57.

32. Vargas, C. A.; Wilhelm, A. A.; Williams, J.; Lucas, P.; Reynolds, K. A.; Riley, M. R., Integrated Capture and Spectroscopic Detection of Viruses. *Applied and Environmental Microbiology* **2009,** *75* (20), 6431-6440.

33. Wood, B. R., The importance of hydration and DNA conformation in interpreting infrared spectra of cells and tissues. *Chemical Society Reviews* **2016,** *45* (7), 1980-1998.

34. (a) Rowse, M.; Qiu, S.; Tsao, J.; Xian, T.; Khawaja, S.; Yamauchi, Y.; Yang, Z.; Wang, G.; Luo, M., Characterization of potent fusion inhibitors of influenza virus. *PLoS One* **2015,** *10* (3), e0122536; (b) Rowse, M.; Qiu, S.; Tsao, J.; Yamauchi, Y.; Wang, G.; Luo, M., Reduction of Influenza Virus Envelope's Fusogenicity by Viral Fusion Inhibitors. *ACS Infect Dis* **2016,** *2* (1), 47-53.

35. Podbilewicz, B., Virus and Cell Fusion Mechanisms. *Annual Review of Cell and Developmental Biology* **2014,** *30* (1), 111-139.

36. (a) Clark, S. M.; Zaug, J. M., Compressibility of cubic white, orthorhombic black, rhombohedral black, and simple cubic black phosphorus. *Physical Review B* **2010,** *82* (13),

134111; (b) Morita, A., Semiconducting black phosphorus. *Applied Physics A* **1986,** *39* (4), 227-242.

37. Takao, Y.; Asahina, H.; Morita, A. J., Electronic Structure of Black Phosphorus in Tight Binding Approach. *J. Phys. Soc. Jpn.* **1981,** *50*, 3362.

38. Asahina, H.; Shindo, K.; Morita, A., Electronic Structure of Black Phosphorus in Self-Consistent Pseudopotential Approach. *Journal of the Physical Society of Japan* **1982,** *51* (4), 1193-1199.

39. (a) Keyes, R. W., The Electrical Properties of Black Phosphorus. *Phys. Rev.* **1953,** *92*, 580; (b) Asahina, H.; Morita, A., Band structure and optical properties of black phosphorus. *Journal of Physics C: Solid State Physics* **1984,** *17* (11), 1839; (c) Rudenko, A. N.; Katsnelson, M. I., Quasiparticle band structure and tight-binding model for single- and bilayer black phosphorus. *Physical Review B* **2014,** *89* (20), 201408.

40. (a) Eckmann, A.; Park, J.; Yang, H. F.; Elias, D.; Mayorov, A. S.; Yu, G. L.; Jalil, R.; Novoselov, K. S.; Gorbachev, R. V.; Lazzeri, M.; Geim, A. K.; Casiraghi, C., Raman Fingerprint of Aligned Graphene/h-BN Superlattices. *Nano Letters* **2013,** *13* (11), 5242-5246; (b) Wang, Q. H.; Kalantar-Zadeh, K.; Kis, A.; Coleman, J. N.; Strano, M. S., Electronics and optoelectronics of two-dimensional transition metal dichalcogenides. *Nat Nano* **2012,** *7* (11), 699-712; (c) Britnell, L.; Ribeiro, R. M.; Eckmann, A.; Jalil, R.; Belle, B. D.; Mishchenko, A.; Kim, Y. J.; Gorbachev, R. V.; Georgiou, T.; Morozov, S. V.; Grigorenko, A. N.; Geim, A. K.; Casiraghi, C.; Neto, A. H. C.; Novoselov, K. S., Strong Light-Matter Interactions in Heterostructures of Atomically Thin Films. *Science* **2013,** *340* (6138), 1311-1314; (d) Ye, Z.; Cao, T.; O'Brien, K.; Zhu, H.; Yin, X.; Wang, Y.; Louie, S. G.; Zhang, X., Probing excitonic dark states in single-layer tungsten disulphide. *Nature* **2014,** *513* (7517), 214-218.

41. Castellanos-Gomez, A., Black Phosphorus: Narrow Gap, Wide Applications. *The Journal of Physical Chemistry Letters* **2015,** *6* (21), 4280-4291.

42. (a) Chen, Z.; Lin, Y.-M.; Rooks, M. J.; Avouris, P., Graphene nano-ribbon electronics. *Physica E: Low-dimensional Systems and Nanostructures* **2007,** *40* (2), 228-232; (b) Castro, E. V.; Novoselov, K. S.; Morozov, S. V.; Peres, N. M. R.; dos Santos, J. M. B. L.; Nilsson, J.; Guinea, F.; Geim, A. K.; Neto, A. H. C., Biased Bilayer Graphene: Semiconductor with a Gap Tunable by the Electric Field Effect. *Physical Review Letters* **2007,** *99* (21), 216802; (c) Oostinga, J. B.; Heersche, H. B.; Liu, X.; Morpurgo, A. F.; Vandersypen, L. M. K., Gate-induced insulating state in bilayer graphene devices. *Nat Mater* **2008,** *7* (2), 151-157.

43. Liu, X. Z.; Galfsky, T.; Sun, Z.; Xia, F. N.; Lin, E. C.; Lee, Y. H.; Kena-Cohen, S.; Menon, V. M., Strong light-matter coupling in two-dimensional atomic crystals. *Nature Photonics* **2015,** *9* (1), 30-34.

44. Li, L.; Yu, Y.; Ye, G. J.; Ge, Q.; Ou, X.; Wu, H.; Feng, D.; Chen, X. H.; Zhang, Y., Black phosphorus field-effect transistors. *Nature Nanotechnology* **2014,** *9* (5), 372-377.

45. Novoselov, K. S.; Falko, V. I.; Colombo, L.; Gellert, P. R.; Schwab, M. G.; Kim, K., A roadmap for graphene. *Nature* **2012,** *490* (7419), 192-200.

46. (a) Gamage, S.; Li, Z.; Yakovlev, V. S.; Lewis, C.; Wang, H.; Cronin, S. B.; Abate, Y., Nanoscopy of Black Phosphorus Degradation. *Advanced Materials Interfaces* **2016,** *3* (12), 1600121-n/a; (b) Gamage, S.; Fali, A.; Aghamiri, N.; Yang, L.; Ye, P. D.; Abate, Y., Reliable passivation of black phosphorus by thin hybrid coating. *Nanotechnology* **2017,** *28* (26), 265201.

47. (a) Low, T.; Roldan, R.; Wang, H.; Xia, F.; Avouris, P.; Martin Moreno, L.; Guinea, F., Plasmons and Screening in Monolayer and Multilayer Black Phosphorus. *Physical Review Letters* **2014,** *113* (10); (b) Favron, A.; Gaufres, E.; Fossard, F.; Phaneuf-Lheureux, A.-L.; Tang,

N. Y. W.; Levesque, P. L.; Loiseau, A.; Leonelli, R.; Francoeur, S.; Martel, R., Photooxidation and quantum confinement effects in exfoliated black phosphorus. *Nat Mater* **2015,** *14* (8), 826-832.

48. Lam, K.-T.; Guo, J., Plasmonics in strained monolayer black phosphorus. *Journal of Applied Physics* **2015,** *117* (11), 113105.

49. Youngblood, N.; Chen, C.; Koester, S. J.; Li, M., Waveguide-integrated black phosphorus photodetector with high responsivity and low dark current. *Nat Photon* **2015,** *9* (4), 247-252.

50. Li, Q.; Zhou, Q.; Niu, X.; Zhao, Y.; Chen, Q.; Wang, J., Covalent Functionalization of Black Phosphorus from First-Principles. *The Journal of Physical Chemistry Letters* **2016,** *7* (22), 4540-4546.

51. (a) Takeshi, Y.; Katsuhiko, F.; Hiroshi, N.; Tetsuo, T., Benefits of Flat Polymer Dielectric Surface Loading Organic Semiconductors in Field-Effect Transistors Prepared by Electrode-Peeling Transfer. *Japanese Journal of Applied Physics* **2003,** *42* (8A), L967; (b) Castellanos-Gomez, A.; Poot, M.; Amor-Amorós, A.; Steele, G. A.; van der Zant, H. S. J.; Agraït, N.; Rubio-Bollinger, G., Mechanical properties of freely suspended atomically thin dielectric layers of mica. *Nano Research* **2012,** *5* (8), 550-557; (c) Zhang, X.; He, Y.; Li, R.; Dong, H.; Hu, W., 2D Mica Crystal as Electret in Organic Field-Effect Transistors for Multistate Memory. *Advanced Materials* **2016,** *28* (19), 3755-3760.

52. Low, C. G.; Zhang, Q., Ultra-thin and Flat Mica as Gate Dielectric Layers. *Small* **2012,** *8* (14), 2178-2183.

53. (a) Shirota, Y.; Kageyama, H., Charge Carrier Transporting Molecular Materials and Their Applications in Devices. *Chemical Reviews* **2007,** *107* (4), 953-1010; (b) Weeks, J. R., The Dielectric Constant of Mica. *Physical Review* **1922,** *19* (4), 319-322.

APPENDICES

Appendix A: MatLab codes used for black phosphorus degradation modelling

Appendix A.1 Sigmoid model for degraded bubble height and volume

A.1.1 Main code

```
clear;
clc;
% ------------------------------------------------------------------------
% Experimental Data


% t is the time (in days) of the experiment
t=[1,4,5,6,7,8,9,12,13,14]'; % for height, volume and area

% These are the height values (in nm)
% M=[4.9,18.4,46.7,74.4,76.3,98,111,122.3,127.6,128.6]';

% These are the volume values (in micron^3)
% M=[2.54023E-7,0.00128,0.00644,0.01986,0.03583,0.13221,0.19848,0.26619,0.28159,0.28717]';

% These are the degraded area(%) values
M=[2,7.3,8,16,46.7,55,74,89,92,95]';

% These are the time(t)/area(M) values for 5x5um coated sample scan
% t=[4,7,12,15,24,39,43]';
% M=[4.43135,7.39021,7.8137,14.54876,16.52442,17.88188,24.3233]';

% End of Experimental Data
% ------------------------------------------------------------------------

% Fitting the data to a logistic function
% ---------------------------------------
tt=0:20; % range for time axis

% initial parameters
 K=10;
 r=0.5;
 t0=5;

% % Plotting the initial fit
% figure(1);
% plot(t,M,'bs',tt,logistic_func(tt,K,r,t0));
% title('Area % vs. Time')
% xlabel('Time (days)')
% ylabel('Area %')

% energy landscape
% using the reduced form, where we solve for K in terms of the other two variables
```

```
num_r=60;
rvec=linspace(.01,.6,num_r);

num_t0=65;
t0_vec=linspace(11,75,num_t0);

penalty_array=zeros(num_t0,num_r);
for i=1:num_t0
   for j=1:num_r
      penalty_array(i,j)=penalty_logistic([rvec(j),t0_vec(i)],t,M);
   end
end
% figure(1)
% mesh(rvec,t0_vec,penalty_array)
% axis tight
% xlabel('r')
% ylabel('t_0')
% ylabel('Penalty Function')

% contour plot of error
% figure(2)
% contour(rvec,t0_vec,penalty_array)
hold on;
% finding the best spot on the contour plot and marking with a star:
[m1,p1]=min(penalty_array);
[m2,p2]=min(m1);
best_r=rvec(p2);
best_t0=t0_vec(p1(p2));
% plot(best_r,best_t0,'*')
hold off
% mytitle=sprintf('Best guess is r=%4.2f, t_0=%5.1f',best_r,best_t0);
% title(mytitle);
% xlabel('r')
% ylabel('t_0')
% colorbar

% Find the best-fit parameters
paramguess=[best_r,best_t0];
params=fminsearch(@penalty_logistic,paramguess,[],t,M);
r=params(1);t0=params(2);
h=1./(1+exp(-r*(t-t0)));
K=dot(h,M)/dot(h,h);

% Plotting the best fit curve
figure(3)
plot(t,M,'o',tt,logistic_func(tt,K,r,t0));
title('Best fit')
xlabel('Time (days)')
ylabel('y (units)')
plot(t,M,'gs',tt,logistic_func(tt,K,r,t0));

% Printing the best fit parameters
fprintf('The best-fit parameters are:\n')
```

```
fprintf('    K=%f\n',K)
fprintf('    r=%f\n',r)
fprintf('   t0=%f\n',t0)

% Plot the residuals
% figure(4);
% residuals= M - logistic_func(t,K,r,t0);
% scatter(t,residuals,'filled');
% xlabel('t (hours)'); ylabel('M_i - M(t_i)')

% ------------------------------------------------------------------------
% RESULTS
% ------------------------------------------------------------------------
% Best parameters for height.
%  K=127.214989;
%  r=0.646526;
%  t0=6.006112;

% Best parameters for volume.
% K=0.278950;
% r=1.274815;
% t0=8.212824;

% Best parameters for area%.
% K=92.752326;
% r=0.866099;
% t0=7.387514;

% Best parameters for area% of 5x5um coated sample scan.
% K=21.058335;
% r=0.130325;
% t0=12.850785;
% ------------------------------------------------------------------------
```

A.1.2 Logistic function version 1

```
function y = logistic_func(t,K,r,t0)
y=K./(1+exp(-r*(t-t0)));
```

A.1.2 Logistic function version 2

```
function z=penalty_logistic(params,t,y)
% This is the function e in equation (95) on page 183
r=params(1);t0=params(2);

h=1./(1+exp(-r*(t-t0)));

numerator  =  -dot(h,y)^2;
denominator =  dot(h,h);
z=numerator/denominator;
```

Appendix A.2 Modified forest fire model for degraded area percentage

A.2.1 Main code

```
clc;
clear;
% defines the grid size (to be defined by the user)
M=200; N=200;

n_s=400000; % number of area elements (to be defined by the user)
ds=M*N/n_s;

tmax=500; % maximum time in days
n_t=tmax+1; % number of time points
dt=tmax/(n_t-1);

% define fit parameters

eta_0=0.025; % tendency of any given site to degrade even without any degraded neighbor sites
delta_eta=15; % neighbor contribution

% defines matrices
G=zeros(M,N);% for 'sample surface'
D=zeros(M,N);% for degradation matrix
P=zeros(M,N);% for probability matrix

% initial value
% t=0; % for degradation percentage
% i=0; % for iteration counter
percent_values=zeros(n_t, 1);
for i=[2:n_t]
% Calculating degradation matrix
   D=DegCal(G);

% Calculating Probability matrix
%     P=ProbCalExp( D, eta_0, delta_eta, dt, ds); % Influence of neighbors is considered
%    P=ProbCalExp_1( D, eta_0, delta_eta, dt, ds); % Influence of neighbors is NOT considered AT ALL
   P=ProbCalExp_2( D, eta_0, delta_eta, dt, ds); % Influence of the NUMBER of neighbors is NOT considered

% disp(sprintf('The probability matrix is'));
% disp(P);

% R=(rand(M,N))<P;%degradation starts
   R=(rand(M,N));

   G(R<P)=1;
   %disp(sprintf('Degradation initiates'));
%     fprintf('Day %d.\n',i);
   s=sum(sum(G));
   t=(s*100)/(M*N); % calculates degradation percentage
%     disp(sprintf('Degraded units = %4.0f',s));
%     disp(sprintf('Degraded percentage = %4.2f %\n',t));
%     percent_values(i)=t;% this accumulates the degradation% values in an array
```

```
%     fprintf(1, '\n');
disp(sprintf(' %4.2f %\n',t));
% prepare to plot the surface
   figure(1);
   colormap([1 1 0;.3 .3 .3]);
   image(100*G);

% exit the loop when degradation completed
   if t==100
   disp(sprintf('Sample is completely degraded'));
   break
   end
   pause(.2); % interval between two iterations
end

disp(sprintf('# of iterations = %4.0f',i));
tt=dt*[0:n_t-1]';
if i<tt
   tt==i;
end
% display experimental values (t=55, M=98 are just 'interpolated' values)
t=[0,1,4,5,6,7,8,9,12,13,14,55,90]';
M=[0,2,7.3,8,16,46.7,55,74,89,92,95,98,100]';

% display fit
figure(2);
plot(t,M, '*',tt,percent_values);
% e=std(M)*zeros(size(t));
% errorbar(t,M,e);
% plot(percent_values);
axis([0 i-1 0 110]) % sets axis limits
set(gca, 'YTick', 0:20:110);
title(['parameters: ' 'dt = ' num2str(dt) ', ds = ' num2str(ds) ', eta-0 = ' num2str(eta_0) ',  delta-eta = '
num2str(delta_eta)]);
xlabel('time (days)')
ylabel('Area %');

% saves the figure
fname = sprintf('sim-fig_%d_%1.1d_%1.1d_%1.1d_%1.1d.jpg', tmax,dt,ds,eta_0,delta_eta);
saveas(figure(2),fname)
```

A.2.2 Function that calculates the degradation matrix

```
function [ D ] = DegCal(G)
%DegCal calculates the degradation matrix of the given grid matrix
   R=size(G);
   M=R(1,1);
```

```
   N=R(1,2);
%     k = [0,1,0;1,0,1;0,1,0];
%     D = conv2(G, k,'same');
   Dr=zeros(M,N);
   Dc=zeros(M,N);
   %Calculating inner cells
   for i=2:M-1;
      for j=2:N-1;
      Dr(i,2:N-1)=G(i-1,2:M-1)+G(i+1,2:M-1);   %inner rows
      Dc(2:N-1,j)=G(2:N-1,j-1)+G(2:N-1,j+1);   %inner columns
      end
   end
   D=Dr+Dc;
   %Calculating first/last columns/rows of degradation matrix
   for i=2:M-1;
      for j=2:N-1;
      D(1,i)=G(1,i-1)+G(2,i)+G(1,i+1);    %First row
      D(j,1)=G(j-1,1)+G(j,2)+G(j+1,1);    %First column
      D(M,i)=G(M,i-1)+G(M-1,i)+G(M,i+1);  %Last row
      D(j,N)=G(j-1,N)+G(j,N-1)+G(j+1,N);  %last column
      end
   end
   %Calculating four corners of degradation matrix
      D(1,1)=G(1,2)+G(2,1);
      D(1,M)=G(1,N-1)+G(2,N);
      D(N,1)=G(M-1,1)+G(M,2);
      D(M,N)=G(M,N-1)+G(M-1,N);
 %-------End of Calculating degradation matrix----%
 %-------------------------------------------------%
 % disp(sprintf('The degradation matrix is'));
% disp(D);

End
```

A.2.2 Functions that calculate the probability matrix for three different cases

```
function [ P ] = ProbCalExp( D, eta_0, delta_eta, dt, ds)
%DegCal calculates the probability matrix of the given degradation matrix
   R=size(D);
   M=R(1,1);
   N=R(1,2);

   for i=1:M;
      for j=1:N;
         eta(i,j)=eta(i,j) +D(i,j)*delta_eta;
         P(i,j)=1-exp(-dt*ds*eta(i,j));
      end
   end
end

function [ P ] = ProbCalExp_1( D, eta_0, delta_eta, dt, ds)
% DegCal calculates the probability matrix of the given degradation matrix
% In this calculation, the influence of the nearest neighbores is NOT AT ALL
% taken in to account
```

```
    R=size(D);
    M=R(1,1);
    N=R(1,2);

    eta=eta_0 * ones(M, N);

    for i=1:M;
        for j=1:N;
            eta(i,j)=eta(i,j);
            P(i,j)=1-exp(-dt*ds*eta(i,j));
        end
    end
end


function [ P ] = ProbCalExp_2( D, eta_0, delta_eta, dt, ds)
% DegCal calculates the probability matrix of the given degradation matrix
% This calculation is independent of the number of degraded neighbors.
% No matter the number of degraded neighbors is 0, 1, 2, 3 or 4, the
% influence considered same.
    R=size(D);
    M=R(1,1);
    N=R(1,2);

    for i=1:M;
        for j=1:N;
            eta(i,j)=eta(i,j) +D(i,j)*delta_eta;
            P(i,j)=1-exp(-dt*ds*eta(i,j));
        end
    end

end
```

Appendix B: Permissions from publishers for reusing the published materials

Appendix B.1 Nanoscopy of Black Phosphorus Degradation

Appendix B.2 Reliable Passivation of Black Phosphorus by Thin Hybrid Coating

IOP Publishing LICENSE
TERMS AND CONDITIONS

Jun 23, 2017

This is a License Agreement between Mr. Sampath Gamage ("You") and IOP Publishing ("IOP Publishing") provided by Copyright Clearance Center ("CCC"). The license consists of your order details, the terms and conditions provided by IOP Publishing, and the payment terms and conditions.

All payments must be made in full to CCC. For payment instructions, please see information listed at the bottom of this form.

License Number	4134731041437
License date	Jun 22, 2017
Licensed content publisher	IOP Publishing
Licensed content title	Nanotechnology
Licensed content date	Jan 1, 1990
Type of Use	Thesis/Dissertation
Requestor type	Publisher, not-for-profit
Format	Print, Electronic
Portion	chapter/article
Title or numeric reference of the portion(s)	Reliable passivation of black phosphorus by thin hybrid coating
Title of the article or chapter the portion is from	N/A
Editor of portion(s)	N/A
Author of portion(s)	S Gamage
Volume of serial or monograph.	28
Issue, if republishing an article from a serial	26
Page range of the portion	
Publication date of portion	8 June 2017
Rights for	Main product
Duration of use	Life of current edition
Creation of copies for the disabled	no
With minor editing privileges	yes
For distribution to	Worldwide
In the following language(s)	Original language of publication
With incidental promotional use	no
The lifetime unit quantity of new product	Up to 499
Made available in the	Academic research

Appendix B.3 Black Phosphorus: Narrow Gap, Wide Applications